MIT Libraries | DSpace@MIT

MIT Open Access Articles

Ab initio GGA+U study of oxygen evolution and oxygen reduction electrocatalysis on the (001) surfaces of lanthanum transition metal perovskites LaBO

The MIT Faculty has made this article openly available. ***Please share*** how this access benefits you. Your story matters.

Citation: Lee, Yueh-Lin, Milind J. Gadre, Yang Shao-Horn, and Dane Morgan. "Ab Initio GGA +U Study of Oxygen Evolution and Oxygen Reduction Electrocatalysis on the (001) Surfaces of Lanthanum Transition Metal Perovskites LaBO3 (B = Cr, Mn, Fe, Co and Ni)." Phys. Chem. Chem. Phys. 17, no. 33 (2015): 21643–21663.

As Published: http://dx.doi.org/10.1039/c5cp02834e

Publisher: Royal Society of Chemistry (Great Britain)

Persistent URL: http://hdl.handle.net/1721.1/110618

Version: Author's final manuscript: final author's manuscript post peer review, without publisher's formatting or copy editing

Terms of use: Creative Commons Attribution-Noncommercial-Share Alike

Massachusetts Institute of Technology

Physical Chemistry and Chemical Physics RSCPublishing

ARTICLE

Ab initio GGA+U Study of Oxygen Evolution and Oxygen Reduction Electrocatalysis on the (001) Surfaces of Lanthanum Transition Metal Perovskites $LaBO_3$ (B=Cr, Mn, Fe, Co and Ni)

Cite this: DOI: 10.1039/x0xx00000x

Received 00th January 2015,
Accepted 00th January 2015

DOI: 10.1039/x0xx00000x

www.rsc.org/

Yueh-Lin Lee[a], Milind J. Gadre[d], Yang Shao-Horn[*a,b,c], Dane Morgan[d*]

In this work, we performed Density Functional Theory (DFT) calculations with inclusion of Hubbard U corrections for the transition metal *d*-electrons, to investigate stability and electrocatalytic activities of the oxygen evolution reaction (OER) and oxygen reduction reaction (ORR) for the ABO_3 (A=La; B= Cr, Mn, Fe, Co, and Ni) (001) surfaces. We showed surface binding energies of relevant ORR/OER species are coupled strongly to surface polarity and local oxidation states, giving large (~1 eV scale per adsorbate) differences in binding between (001) AO and BO_2 surfaces, where the more oxidized BO_2 bare surfaces in general exhibit weak coverage dependence, while the more reduced AO bare surfaces of the $LaCrO_3$, $LaMnO_3$, and $LaFeO_3$ perovskites with lower *d*-electron filling show strong/moderate coverage dependences. We then predicted that surface coverage can play a key role in determining surface stability, and when coverage effects are included the AO and BO_2 (001) surfaces have either similar stability or the AO surface is more stable, as found for 1 monolayer HO* covered AO surfaces of $LaCrO_3$ and $LaFeO_3$ under ORR conditions and 1 monolayer O* covered $LaNiO_3$ AO surface under OER conditions. For the (001) AO surfaces with strong coverage dependent surface adsorption, we predicted a decrease in ORR overpotential of 1~2 V with proper treatment of coverage effects as compared to those of the bare surface simulations. Our results indicated that the GGA+U method and proper treatment of coverage effects more accurately predict ORR and OER overpotentials relative to experimental values as compared to the GGA method and bare surfaces. The overall ORR activity trends vs. the $LaBO_3$ series were predicted to be Co>Mn≈Ni>Fe>Cr.

A Introduction

Search and design of highly active and less expensive materials for catalyzing the sluggish kinetics of the oxygen reduction reaction (ORR) and the oxygen evolution reaction (OER) is of primary importance in many electrochemical energy device applications such as direct-solar and electrolytic water splitting, metal-air batteries, and fuel cells[1-6]. In replacement of noble metal containing catalysts, first row transition-metal perovskites are promising candidate materials for catalyzing OER and ORR in alkaline solution. A number of activity descriptor approaches provide an efficient and practical guidance to facilitate screening of alternate perovskite OER and ORR catalysts[4, 5, 7], such as number of *d*-electrons [1, 8], oxidation enthalpy[1, 9], the *p*-band center relative to the Fermi level[6], the degree of overlapping between the e_g orbitals of the M(3*d*) band and the O(2*p*) band relative to the Fermi level[10], and free energies of formation of the bulk perovskites relative to metal and H_2O/H_2[11]. However, there are still many questions about surfaces and interfaces of the transition-metal perovskite catalyst systems in the aqueous environment under the OER and ORR conditions which have invoked further experimental studies[12, 13]. These questions include, *e.g.*, what are the stable surfaces for these perovskites, how different surface orientations/terminations result in different activities, how the bulk electronic structure descriptors can be used to describe activities of various surface terminations, and whether/how surface stability is linked to surface catalytic activities. First principles-based Density Functional Theory (DFT) methods are now able to simulate catalytic reactions at specific metal oxide surfaces and extract surface electronic structure and energetic details, which can provide new insights into structure-activity relationships and strategies for material design and development[7, 14-16]. For example, Man *et al.*[14] have performed

This journal is © The Royal Society of Chemistry 2013

DFT-RPBE (revised Perdew-Burke-Ernzerhof GGA functional[17]) calculations on ABO_3 (A=Sr and La, B=Sc~Cu) perovskite (001) BO_2 surfaces and showed a linear correlation between the predicted theoretical overpotential (η_{the}) vs. experimental data (η_{exp}) for OER on $LaMnO_3$, $LaFeO_3$, $LaCoO_3$, and $LaNiO_3$[1]. The reaction free energies based on the calculated surface adsorption energies also rendered mechanistic information regarding the rate-limiting step for OER and ORR on a given material surface[14]. However, DFT calculations at the Local Density Approximation (LDA) or Generalized Gradient Approximation (GGA) level are known to produce errors describing energetics of transition metal oxides [18-20], which adds additional complications in predicting electrocatalytic activities of correlated electron materials directly from the standard DFT modeling. To correct the error associated with the correlated electrons in transition metal oxides, recent theoretical works adopted improved exchange-correlation functionals such as the DFT+U method[18] or hybrid functionals[21] to investigate surface adsorption properties and activities of transition metal oxide surfaces for the OER and ORR. For example, Garcia-Mota *et al*. [22] have reported the importance of including Hubbard U corrections[18] for describing Co_3O_4 and β-CoOOH surface OER activities. The Hubbard-U correction shifts the location of Co_3O_4 and β-CoOOH from the strong binding leg to the weak binding branch of the OER volcano plot, and lowers activity of both Co_3O_4(001) and β-CoOOH($01\bar{1}\bar{2}$) as compared to the results computed at the GGA level. Focusing on transition metal perovskites, Wang *et al.*[15] performed a comparative DFT study using the standard GGA, GGA+U, and hybrid functional methods, and reported that the predicted theoretical ORR activity calculated using the hybrid functional for the bare (001) BO_2 surfaces are in the following order $LaMnO_3 > LaCrO_3 > LaFeO_3$, in contrast to the GGA prediction of $LaMnO_3 \approx LaFeO_3 > LaCrO_3$. Although these recent studies have demonstrated that improved exchange-correlation functionals yield significantly different results than traditional LDA/GGA approaches, these more advanced models have not yet been applied to develop a realistic model of the stable surfaces and their coverage under catalytic conditions. Such effects have been shown to cause significant changes in the predicted ORR activity of Ni metal[23]. Furthermore, detailed experimental characterizations[24] has also observed a correlation between the surface HO* coverage and the ORR activities of $LaBO_3$ (001) films (B=Cr, Mn, Fe, Co, and Ni). Overall, the effects of surface stability[6, 12, 25], termination and polarity[26, 27] and coverage on the OER and ORR activities still remain largely unexplored.

In this work, we performed a systematic study combining the DFT+U approach, the thermodynamic overpotential method[14, 28], and perovskite bulk and (001) surface stability analysis, to predict both OER and ORR activities on the $LaBO_3$ perovskite (001) AO and BO_2 surfaces (B=Cr, Mn, Fe, Co, and Ni) at their stable surface coverage within the concerted proton-electron transfer scheme[29]. We examined the stability of ideally truncated (001) AO and BO_2 surfaces as well as the surfaces at various coverage of HO*, O*, HOO* (adsorbed above a metal site or between two metal sites) and H* (adsorbed on surface O) close to the ORR and OER conditions. We then investigated the HO*, O*, and HOO* adsorption energies on the stable (001) AO and BO_2 surfaces to construct the OER and ORR volcanoes as functions of free energy descriptors, and predicted the OER and ORR activities self-consistently at these stable surfaces. We showed surface binding energies of relevant ORR/OER species are coupled strongly to surface polarity and local oxidation states, giving large (~1 eV scale per adsorbate) differences in binding between (001) AO and BO_2 surfaces. We also showed that the sub-surface layer O *2p*-band centers showed an excellent correlation with the surface HO* adsorption energies of all the (001) bare surfaces for the investigated perovskites. Upon including the stable coverage with the DFT+U method, the predicted OER and ORR thermodynamic overpotentials exhibit reduced absolute error vs. the experimental values[4, 5] as compared to calculations on bare surfaces at the GGA level[14]. In addition, we distinguished systems with strong vs. weak coverage dependent surface properties, and demonstrated the predicted ORR overpotentials on the (001) AO surfaces with strong coverage dependent surface adsorption can be significantly altered (by 1~2 V) relative to those predicted at the bare surfaces at high coverage of HO*. Our self-consistent thermodynamic analysis results suggest that the predicted ORR activities at the stable (001) BO_2 and AO surfaces are much closer than for the bare surfaces, and values on both self-consistently modeled surfaces are within 0.25 V. Overall, our integrated *ab initio* thermodynamic framework allows determinate of bulk/surface stability, termination, and coverage of perovskites, and catalytic activities on equilibrium surfaces under the OER and ORR conditions. These results yield insights to surface structure–activity relationships for rational development of perovskite materials with desired surface functionalities for OER and ORR.

B Computational Methods

1 Density Function Theory (DFT) Modeling Approach

Spin polarized DFT calculations were performed with the Vienna Ab-initio Simulation Package (VASP)[30]. We used a plane wave basis set, the GGA-Perdew-Wang-91[31] exchange correlation function, and the Projector Augmented Wave (PAW) method[32], with electronic configurations La (5s2 5p6 6s2 5d1), Sr (5s2 4p6), O_s (soft oxygen pseudopotential, 2s2 2p4), B = Cr_{pv} (3p6 3d5 4s1), Mn_{pv} (3p6 3d6 4s1), Fe_{pv} (3p6 3d7 4s1), Co (3d8 4s1), and Ni_{pv} (3p6 3d9 4s1). All calculations were performed with an energy cut-off of 450 eV.

For the GGA+U calculation, we used the standard Dudarev implementation[33], where the on-site Coulomb interaction for the localized transition metal d orbitals was parametrized by $U_{eff} = U - J$ with the Perdew-Wang-91 functional. Optimized U_{eff} for the metal atoms in $LaBO_3$ (U_{eff} = 3.5, 4, 4, 3.3, and 6.4 eV for Cr, Mn, Fe, Co, and Ni, respectively) were taken from References [19, 34]. These optimial U_{eff} were determined by fitting to oxidation enthalpies of binary transition metal oxides and have been shown to provide improved accuracy in the calculated formation enthalpies of $LaBO_3$ perovskites relative to the binary metal oxides as compared to formation enthalpies calculated with the GGA approach.[34]

Full optimization of bulk perovskite calculations for each $LaBO_3$ (B = Cr, Mn, Fe, Co, and Ni) were performed using the experimental symmetry at low temperature[35]. Magnetic structure was set as ferromagnetic ordering [36] for B = Cr, Mn, Co as a consistent and tractable approach to approximate the paramagnetic state at room temperature. For B = Fe we used a G-type anti-ferromagnetic (AFM) ordering as $LaFeO_3$ has a Néel temperature above room temperature and we expect the

 This journal is © The Royal Society of Chemistry 2012

material to be magnetically ordered at room temperature OER and ORR conditions [36]. The (001) slabs were constructed with surface-plane lattice constants obtained by taking the cube root of the normalized volume (per formula unit) of the fully relaxed perovskites, along with a 10 Å vacuum space inserted between the two truncated surface terminations and removal of a BO_2 layer for the 7-layer (001) AO slab (and removal of an AO layer for the 7-layer (001) BO_2 slab), as shown Figure 1. The fully relaxed perovskite bulk coordinates were used as initial starting atomic positions in the slab models to restore the distortion of the metal-oxygen octahedra. Internal relaxations of the (001) slab coordinates were first performed without adsorbates. We note that the adopted vacuum thickness and slab thickness were previously shown to provide converged surface energy as well as defect formation energies with an accuracy of ~0.1 eV/defect for the $LaMnO_3$ (001) surfaces[27, 34]. In addition, for the perovskite systems with band gaps such as $LaFeO_3$, the nonstoichiometry of the symmetric slab forces surface charge equal to half of the bulk layer charge, which is equivalent to the surface compensating charge to the bulk polarity that would come from the large bulk-like region of a thick film, resulting in thickness independent surface energy[27]. Therefore, the adopted surface models can be considered as the thick film conditions. The adsorbates (HO*, O*, HOO*, and H*) were then adsorbed on one side of the slab and the adsorbate coverage has been varies from ¼ to 1 monolayer (ML), where 1 ML corresponds to one adsorbate per (1×1) (001) surface (*i.e*, 1 ML is one absorbate per one BO_2 or AO unit). The bottom two layers of the slab models were kept fixed, while the adsorbate and remaining slab coordinates were internally relaxed. A (2×2×1) *k*-point sampling was used for such slab models. Dipole corrections[37] were included in the surface calculations to remove errors associated the surface dipole moment in periodic boundary condition calculations.

2 Bulk phase diagram and oxygen chemical potential:

Spin polarized DFT calculations were performed with the Vienna Ab-initio Simulation Package (VASP)[30]To determine $LaBO_3$ perovskite phase stability vs. applied potential and pH, we performed calculations for La, Cr, Mn, Fe, Co, and Ni metal and a series of binary transition metal oxides. The chemical potential of oxygen μ_O at a given potential relative to the standard hydrogen electrode (SHE), following the computational SHE method[14, 28], can be defined as:

$$\mu_0 = \left[E_{DFT}(H_2O^{(g)}) + ZPE_{H_2O} - TS^0_{H_2O^{(g)}}(0.035\ bar)\right] - \left[E_{DFT}(H_2^{(g)}) + ZPE_{H_2} - TS^0_{H_2^{(g)}}\right] + 2\left(k_bT\ln a_{H^+} - e\phi\right) \quad \text{Eqn. 1}$$

where $E_{DFT}(H_2O^{(g)})$ and $E_{DFT}(H_2^{(g)})$, $ZPE_{H_2O^{(g)}}$ and $ZPE_{H_2^{(g)}}$, and $S^0_{H_2O^{(g)}}$ and $S^0_{H_2^{(g)}}$, are the calculated DFT energy, the zero point energy, and the entropy of gas phase H_2O and H_2, respectively. T is the room temperature, and ϕ is the applied potential.

In the following discussion, we describe how the bulk perovskite phase diagram was constructed in this work. We note the vibrational contributions in the chemical potential of metals and oxygens in the solid phase were neglected in our analysis, considering the low (room) temperature condition in the experiments. We will make use of the thermodynamic constraint that is given by the fact that the oxide is in equilibrium with its constituents. This relates the calculated DFT total energy of the ABO_3 perovskite, $E^{ABO_3}_{DFT}$ (normalized as per formula unit) to chemical potentials through[38]:

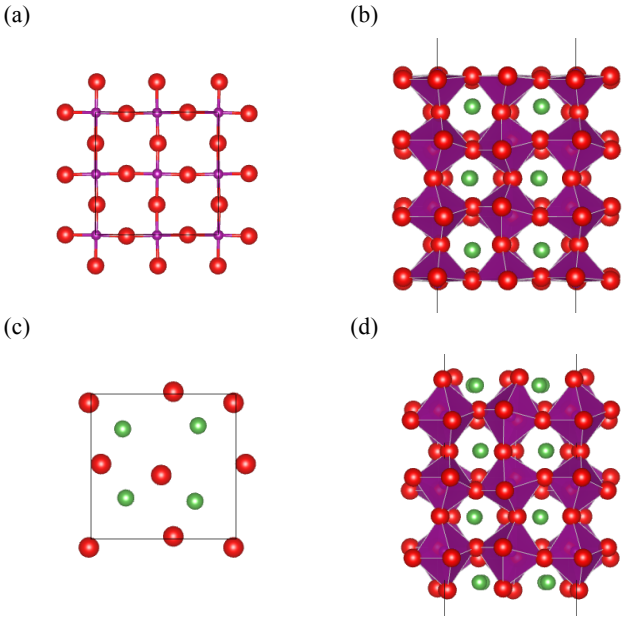

Figure 1. The adopted $LaBO_3$ (001) BO_2 and AO slab models: (a) top view of the top (001) BO_2 surface layer, (b) side view of the symmetric 7-layer (001) BO_2 slab, (c) top view of the top (001) AO surface layer (d) side view of the (001) AO slab.

$$1\cdot\mu_j^{ABO_3} + 1\cdot\mu_R^{ABO_3} + 3\cdot\mu_O(\phi, pH) = E_{DFT}^{ABO_3} \quad \text{Eqn. 2}$$

where $\mu_j^{ABO_3}$ is the chosen independent chemical potential of metal *j* constituent in the ABO_3 perovskites, $\mu_R^{ABO_3}$ is the remaining dependent chemical potential of metal *R* constituent in the ABO_3 perovskites a given applied potential ϕ and pH. We note for $LaFeO_3$, only the ground state G-type AFM configuration is used to represent the total energy of the bulk perovskite phase.

The relevant phase diagrams can now be plotted using bulk μ_O (set by ϕ and pH) and μ_j as independent chemical potential degree of freedom (in this work we choose La as the independent metal chemical potential), and at any point on the bulk phase diagram surface energies of various surface configurations can be calculated using the bulk chemical potentials as the references[39, 40]. These surface energies can then be used to examine relative stability among various surface terminations.

To further constrain the bulk perovskite stable chemical potential region in the phase diagram, we included a set of

chemical potential boundary lines of lower-order binary metal oxides. These boundary lines represent equilibrium between bulk perovskite and a binary metal oxide compound. For binary metal oxides, the chemical potential of metals can also be expressed by the following equation:

$$\mu_M^{MO_x} = E_{DFT}^{MO_x} - x \cdot \mu_O(\phi, pH) \qquad \text{Eqn. 3}$$

where M denotes the metal element (La, Cr, Mn, Fe, Co, and Ni in this work), and $E_{DFT}^{MO_x}$ is the DFT total energy of a metal binary oxide. To prevent precipitation of lower order binary metal oxides from a perovskite at a given μ_O (set by ϕ and pH), the chemical potential of a metal constituent in the perovskite has to be smaller than that in the lower order binary metal oxide compound:

$$\mu_M^{ABO_3} < \mu_M^{MO_x} \qquad \text{Eqn. 4}$$

The inequality equations can be used to constrain the stable chemical potential region in the bulk perovskite phase diagram and to constrain the range of bulk metal references used to examine stability of various surface termination and configurations at a given condition of metal chemical potential, applied potential ϕ, and pH. We note that our thermodynamic analysis is within the scheme of the concerted proton-electron transfer[29], where transfer of single (or multiple) proton and electron occurs in a concerted elementary step, instead of step-wise mechanisms in which the electron and proton are transferred sequentially. Consequently, all equilibrium potentials of (electrochemical) reaction steps contain the same $G(H^+)/e_0$ term ($G(H^+)$ is the free energy of proton and e_0 is the magnitude of its charge) and the activities/overpotentials of catalysts exhibit no pH dependences[23]. The stability of solvated metal ionic species, which requires decoupling of protons and electrons in reaction free energies (relative to the SHE reference) and incorporation of available experimental data for free energies of solvated metal ionic species vs. solid states[41], are not included in this work. Therefore, for simplicity the corresponding pH in this work is referred to the experimental condition, *i.e.* pH=13 [4, 5] and only applied voltage vs. RHE is presented in the x-axis of the plots. While only lower order binary metal oxides were included for accessing the perovskite bulk stability region in alkaline solution close to pH=12~14, the binary metal oxides for Cr~Ni close to the ORR/OER potential regime are in general the stable phases except for Cr under the OER conditions[42, 43]. Other phases such as hydroxides or solvated metal ion species were not considered in our stability analysis but could be incorporated in future work to refine the bulk perovskite phase stability diagram[44, 45]. However, our purpose here is not to assess bulk stability, but merely to supply reasonable ranges of chemical potentials for assessing the stability of different surface terminations. Including additional phases would only reduce the range of chemical potentials available and would not alter the predicted surface stabilities. For more details of the DFT-based Pourbaix (E-pH) diagram construction for complex oxides, we refer to Refs. 44, 45.

In Figure 2, we show bulk perovskite stability diagram at a given potential condition in alkaline solution (at pH=13) presented based on chemical potential of La (y-axis) and chemical potential of oxygen (x-axis). The chemical potential of oxygen can be expressed in terms of the applied potential at a given pH following Eqn. 1. Each thin line represents an equilibrium between the perovskite oxide and a given lower order oxide compound, while the shaded area in the plots is the region where the perovskite oxide is stable relative to the lower order binary oxide compounds. The results shown in Figure 2 are mainly to provide the information regarding the stable perovskite metal chemical potential boundary conditions constrained by the precipitation lines of the binary metal oxides. The stable chemical potential ranges will be further used below for determination of surface energy of the investigated perovskite systems.

3 Surface stability analysis:

The surface calculations for the perovskite (001) BO_2 and AO terminations were performed with the 7-layer (001) slabs with (2×2) surface area, as shown Figure 1. The relative stability of the (001) AO and BO_2 surfaces under a given applied potential and pH were calculated based on the following equations:

$$\Gamma_i = \frac{1}{2A_S}[E_{total}^i - N_O \cdot \mu_O(\phi, pH) - N_j \cdot \mu_j^{ABO_3} - N_R \cdot \mu_R^{ABO_3}] \qquad \text{Eqn. 5}$$

where Γ_i is the surface energy, i denotes the type of the slab model ((001) BO_2 or AO slabs in this work), A_s is the surface area of the (2×2) (001) slab (a factor of 2 in front of A_s is to account for two surface terminations per slab), E_{total}^i is the calculated total energy of the slab, N_O is the number of oxygen atoms in the slab, $\mu_O(\phi, pH)$ is the oxygen chemical potential as defined in Eqn. 1, $\mu_j^{ABO_3}$ is the chosen independent chemical potential of metal j constituent in the ABO_3 perovskites, and N_j is the number of the j metal constituent in the slab. As defined in Eqn. 2, $\mu_R^{ABO_3}$ is the remaining dependent chemical potential of metal R constituent in the ABO_3 perovskites and N_R is the number of the R metal constituent in the slab.

To investigate the surface adsorption properties and their coverage dependences (normalized as per adsorbate), we extracted the surface adsorption energies, $\Delta\bar{E}$(X=HO*, O*, HOO*, and H*), at various coverage between θ=0.25 ~ 1.0, *i.e.* $N=1 \sim 4$ in Eqn. 6 (H* is adsorbed at surface terminated oxygen of the (001) surfaces, in contrast to the adsorption site of the other HO*/O*/HOO* species, which are bound with a metal cation or between 2 surface metal cations):

$$\Delta\bar{E}(X^*) = \frac{E_{DFT}^{X^*}(N) - E_{DFT}^*}{N} - \left(a_{X^*} \cdot E_{DFT}^{H_2O} - \frac{b_{X^*}}{2} \cdot E_{DFT}^{H_2}\right) \qquad \text{Eqn. 6}$$

where N is the number of the X^* adsorbed on the simulated (2×2) (001) surfaces, $E_{DFT}^{X^*}(N)$ is the calculated DFT total

This journal is © The Royal Society of Chemistry 2012

energy of the (001) slab with N adsorbed X*s on the surface, E^{*}_{DFT} is the calculated DFT total energy of the ideal (001) slab, a_{X^*} is the number of H_2O and b_{X^*} is the number of H_2 divided by 2 to be used as the reference energies for the adsorbed species.

The stability of the (001) surface AO and BO_2 terminations containing the adsorbed species X*, $\Gamma_i^{X^*}$, was assessed by combining the adsorption free energies normalized by surface area plus the surface energies of the ideally truncated surface terminations:

$$\Gamma_i^{X^*} = \Gamma_i + \frac{\Delta\bar{G}(X^*)\cdot\theta}{A_S} \qquad \text{Eqn. 7}$$

where Γ_i is the surface energy of the ideal (001) surface i (the (001) AO or BO_2 surface), $\Delta\bar{G}(X^*)$ is the surface adsorption free energy normalized as per adsorbate, X* refers to surface adsorbed intermediates, *i.e.* HO*, O*, HOO* and H*, and θ is the surface coverage defined as per (1x1) perovskite (001) surface. The $\Delta\bar{G}(X^*)$ can be expressed by the following equation:

$$\begin{aligned}\Delta\bar{G}(X^*) = {} & \frac{E^{X^*}_{DFT}(N) - E^{*}_{DFT}}{N} \\ & -\left(a_{X^*}\cdot E^{H_2O}_{DFT} - \frac{b_{X^*}}{2}E^{H_2}_{DFT}\right) \\ & + b_{X^*}\cdot\left(k_bT\ln a_{H^+} - e\phi\right) \\ & + ZPE(X^*) - T\cdot\Delta S(X^*) + E_{solv}(X^*)\end{aligned} \qquad \text{Eqn. 8}$$

where ΔZPE(X*) is the zero point energy change of X* on the surface relative to that of the H_2O and H_2 references, ΔS(X*) is the entropy change of X* relative to that of the H_2O and H_2 references, and E_{solv}(X*) is the solvation energy correction for the adsorbed species X*. Note that we treat the absorbed molecules as an ideal mixture (no ordered phases or phase separation is considered) on the surface. However, no explicit free energy of mixing contribution is included in Eqn. 7 as that magnitude of this term (given by k_bT•ln(θ)) is small at room temperature compared to the other energies in the problem. These additional treatments are needed to convert the calculated DFT energies, $\Delta\bar{E}$(X*), into free energies $\Delta\bar{G}$(X*)s. In this study, the zero point plus the entropy terms, ΔZPE(X*)-$T\Delta S$(X*), were taken from the tabulated values in Refs. [14, 16, 28], where energy corrections added to the DFT binding energy for adsorbed HO*, O*, HOO*, and H* are 0.35, 0.05, 0.40, and 0.24 eV, respectively.

The role of solvation effects on the adsorbed species have been shown to cause a significant influence on the free energy surface of the ORR on Pt surfaces[46] as well as stabilizing adsorbed metal oxo-species for transition metal oxide clusters [47, 48]. However, computation of the solvation free energy corrections is not straightforward and requires further validation of the models with experiments[47, 48]. The solvation free energy corrections, E_{solv}(X*), for adsorbed HO*, O*, HOO*, and H* species calculated with the implicit Poisson-Boltzmann model were provided in Ref. 46. These values were utilized in the work by Wang *et al.*[15] for predicting the ORR overpotentials on the (001) BO_2 surface of $LaCrO_3$, $LaMnO_3$, and $LaFeO_3$ calculated using the GGA, GGA+U, and hybrid functional methods. In this work, we followed Wang *et al.*[15] in making the approximation of using the solvation free energy calculated for adsorbed species on the Pt surfaces for the transition metal perovskite surfaces. We note that at high coverage the extended adsorbates covered surfaces may form hydrogen bond network, which can result in double counting of the solvation effect upon adding the E_{solv}(X*) term obtained from the implicit solvation model. However, separation of surface adsorption sites is 3.8~4.0 Å for the perovskite (001) surfaces at 1ML (per metal site) adsorbate coverage, which in general provides a greater distance than the hydrogen bond and supresses such hydrogen bonding effect. For example, the scaling relation between HO* and HOO*, as will be discussed below in Section D1, still holds at high coverage, within an error bar of ±0.2 eV per adsorbate, as shown in Figure S1 of Supporting Information, which indicates that contribution from hydrogen bond network between HOO* adsorbates at the simulated high coverage is still within the ±0.2 eV error bar. To further discern these effects within the ±0.2 eV per adsorbate, additional works that include explicit solvation models or coupling of multiple models with molecular dynamics simulation are needed to better treat interaction between water and adsorbates with statistical determination of the adsorption free energies[49]. In addition, use of improved functionals that include long-range dispersion interactions, which are not treated well at the GGA level, could also improve the model accuracy, since these interaction has been shown to influence both stability of water and predicted absorption potentials[50]. Such aspects are beyond the scope of the present work but important to consider for future studies. That said, the comparison of theoretical activity trends among different systems pursued here may benefit from some degree of error cancellation, reducing the impact of the approximations that have been made in this work.

We also note that the H* adsorption in this study is located at different surface adsorption sites (terminal surface oxygen) from those of the OER/ORR HO*/O*/HOO* reaction intermediate species (bound with metal sites). The coupling of the H* and HO*/O*/HOO* reaction intermediate species may occur, *e.g.*, surface may be stabilized with mixtures of H* at the surface O sites and HO*/O*/HOO* at the surface metal adsorption sites but we only included H* covered surfaces when these surfaces were predicted to be the stable surfaces where the ORR/OER reaction steps (HO*/O*/HOO*) were simulated with H* as spectator species on the surfaces to keep the complexity manageable in the present work.

4 Construction of Theoretical ORR/OER Volcanoes:

4.1 Bare surfaces with weak coverage dependent adsorption properties

For the (001) bare surfaces that exhibit weak coverage dependences in surface adsorption energies for the OER/ORR reaction intermediates (HO*, O*, and HOO*, see Table 1), under the approximation of Langmuir-type surface adsorption (*i.e.*, no interactions between surface species) is appropriate. Within this approximation the predicted OER/ORR potentials are largely independent of their HO*/O*/HOO* surface coverage. In order to examine the effect of Hubbard U correction on the predicted OER/ORR activities, we followed

the previous studies[14, 15] using computational thermodynamic overpotential method[14, 28] to construct OER and ORR volcanoes based on the ideally truncated perovskite (001) surface HO*, O*, and HOO* adsorption energies simulated at 1/4 ML coverage. The OER and ORR theoretical volcanoes can be plotted using the free energies of the reaction steps (established through conversion of the calculated ΔE(HO*), ΔE(O*) and ΔE(HOO*) to ΔG(HO*), ΔG(O*) and ΔG(HOO*)) vs. a surface adsorption free energy descriptor[7, 16, 28]. We note that in such analysis, the effect of H* coverage (adsorbed on the surface O site) was neglected. Neglecting H* covered surfaces for the OER was justified by the surface stability analysis (see Section C.3 below), where H* covered surfaces were in general shown to be unstable. On the other hand, the H* covered (001) BO_2 surfaces were predicted to be stable surfaces under the ORR conditions (see Section C.4 below). Therefore to reach thermodynamic self-consistency as well as to investigate the influence of coverage effect on the predicted ORR activities, additional assessment was performed on the stable adsorbate covered (001) surfaces, including both the stable H* coverage on the (001) BO_2 surfaces and the stable HO* coverage on the (001) AO surfaces, which will be addressed in next section 4.2.

4.2 Surfaces with strong coverage dependent adsorption properties

In some cases we found (consistent with previous works[51, 52]) that the adsorbates interact strongly and adsorption energies have a strong dependence on the adsorbate coverage. To treat such coverage dependence, Hansen *et al.*[23] performed a thermodynamic assessment on stability of Pt, Ag, and Ni (111) surfaces with the most stable adsorbed intermediates to reach self-consistency in both the stability and catalytic activity of the transition metal (111) surfaces for ORR. In Section D.4 below, we performed a self-consistent thermodynamic assessment to predict the ORR activities at stable coverage of the (001) surfaces, including both the stable H* (reducing adsorbate) coverage on the (001) BO_2 surfaces and HO* (oxidizing adsorbate) coverage on the (001) AO surfaces, to illustrate the role of the coverage effect in the predicted ORR activity for $LaBO_3$ perovskites.

The coverage effect for OER was studied for only a subset of systems, namely the (001) BO_2 surfaces of all the $LaBO_3$ systems and the (001) AO surfaces of $LaCoO_3$ and $LaNiO_3$. These surfaces were chosen as they were shown to be the stable surfaces or at least comparably stable surfaces under the OER conditions (see Section D.3 below). Furthermore, they all show weak coverage dependence and their coverage dependence could be readily approximated using their low coverage results. For these surfaces the surface adsorption effects for HO*/O*/HOO* were considered, but not the effects of H*, as H* coverage was shown to be irrelevant under OER conditions (see Section D.3 below). We note that some systems that showed strong coverage dependences in their surface adsorption were also found to suffer from bulk instability issues (*e.g.* for stoichiometric $LaCrO_3$ and $LaMnO_3$ (see Section D.3)), and these systems require further work to refine their bulk chemical potential references as well as surface stability.

C Results- Surface Stability Analysis

1. Surface energy of the bare (001) AO and BO_2 terminations:

The surface stability analysis results shown in Figure 2 provide the relative stability information of the two bare (001) AO and BO_2 surfaces within the stable bulk perovskite chemical potential region, where the grey shaded area with dotted line in the plots represents the predicted stability region of the $LaBO_3$ bulk relative to the binary metal oxide compounds. Stability boundary of the bare (001) BO_2 surface vs. the bare (001) AO

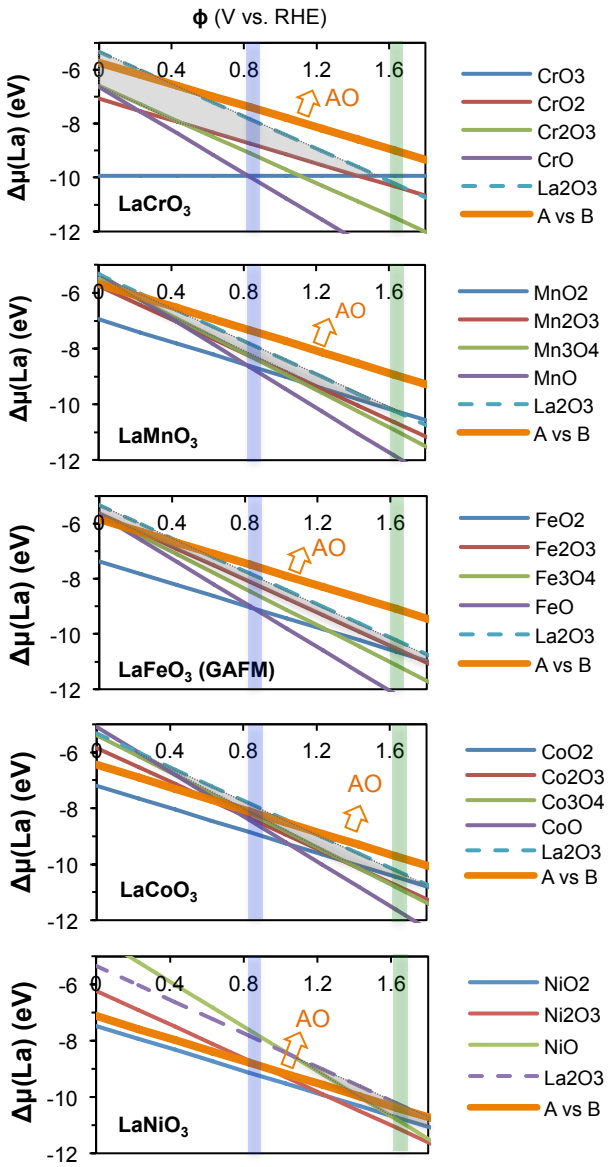

Figure 2. The GGA+U $LaBO_3$ (B= Cr, Mn, Fe-GAFM, Co, and Ni) bulk perovskite phase diagram as functions of applied potential vs. RHE (x-axis, *i.e.*, oxygen chemical potential) and the La chemical potential relative to La metal (y-axis). The grey shaded area with dotted line in the plots shows the predicted stability region of the $LaBO_3$ bulk relative to the binary metal oxide compounds. Stability boundary of the ideal (001) BO_2 surface vs. the ideal (001) AO surface is presented with the thick orange line, where above (below) the line the AO surface (BO_2 surface) is more stable than the (001) BO_2 surface (AO surface). The vertical blue and green shaded area represents the ORR and OER conditions investigated in this work (*i.e.* 0.83 V vs. RHE for ORR and 1.63 V vs. RHE for OER).

This journal is © The Royal Society of Chemistry 2012

surface is presented with the thick orange line, whereas the AO surface (BO_2 surface) is more stable than the (001) BO_2 surface (AO surface) above (below) the orange thick line. We find that the BO_2 termination is in general more stable than or at least comparable to the AO termination under the OER (vertical green shaded area) and ORR (vertical blue shaded area) conditions, except that the AO surface is more stable for $LaNiO_3$ under the ORR condition. Nonetheless, in the DFT modeling the truncated $LaBO_3$ (001) polar surfaces are forced to be compensated intrinsically by modification of surface charge, while in reality the perovskite surfaces can interact with the adsorbed species in the aqueous environment under the ORR and OER conditions. Therefore, it is possible that distinct surface-adsorbate interactions between two ideal (001) AO and BO_2 terminations can alter relative stability of the (001) AO and BO_2 surface terminations upon being covered with stable adsorbates, which will be discussed below in Section C.2.

2. Surface adsorption energies and the coverage dependences:

In Figure S1 of Supporting Information, we show $\Delta\bar{E}(HO^*)$ (top panel), $\Delta\bar{E}(O^*)$(second panel), $\Delta\bar{E}(HOO^*)$(third panel), and $\Delta\bar{E}(H^*)$(bottom panel), vs. θ for the (001) AO (red) and BO_2

Table 1. Summary of the coverage dependences for surface adsorption of HO*/O*/HOO* (oxidizing adsorbates) and H* (reducing adsorbates at surface layer O sites) of the perovskite (001) AO and BO_2 surfaces. The strength of the coverage dependence is determined by the slope of the computed DFT surface adsorption energy vs. surface coverage results shown in Figure S1, Supporting Information. The weak, moderate, and strong coverage dependences are defined as slopes of < 0.2 eV/ML, 0.2~0.5 eV/ML, and > 0.5eV/ML, respectively.

$LaBO_3$ surfaces		HO*/O*/HOO*	H* (at surface O)
$LaCrO_3$	(001) AO	**Strong**	--
	(001) BO_2	Weak	Strong
$LaMnO_3$	(001) AO	**Strong/Moderate**	--
	(001) BO_2	Weak	Strong
$LaFeO_3$ (GAFM)	(001) AO	**Strong**	--
	(001) BO_2	Weak	Strong
$LaCoO_3$	(001) AO	Weak	--
	(001) BO_2	Weak	Strong/moderate
$LaNiO_3$	(001) AO	Weak	--
	(001) BO_2	Weak	Weak

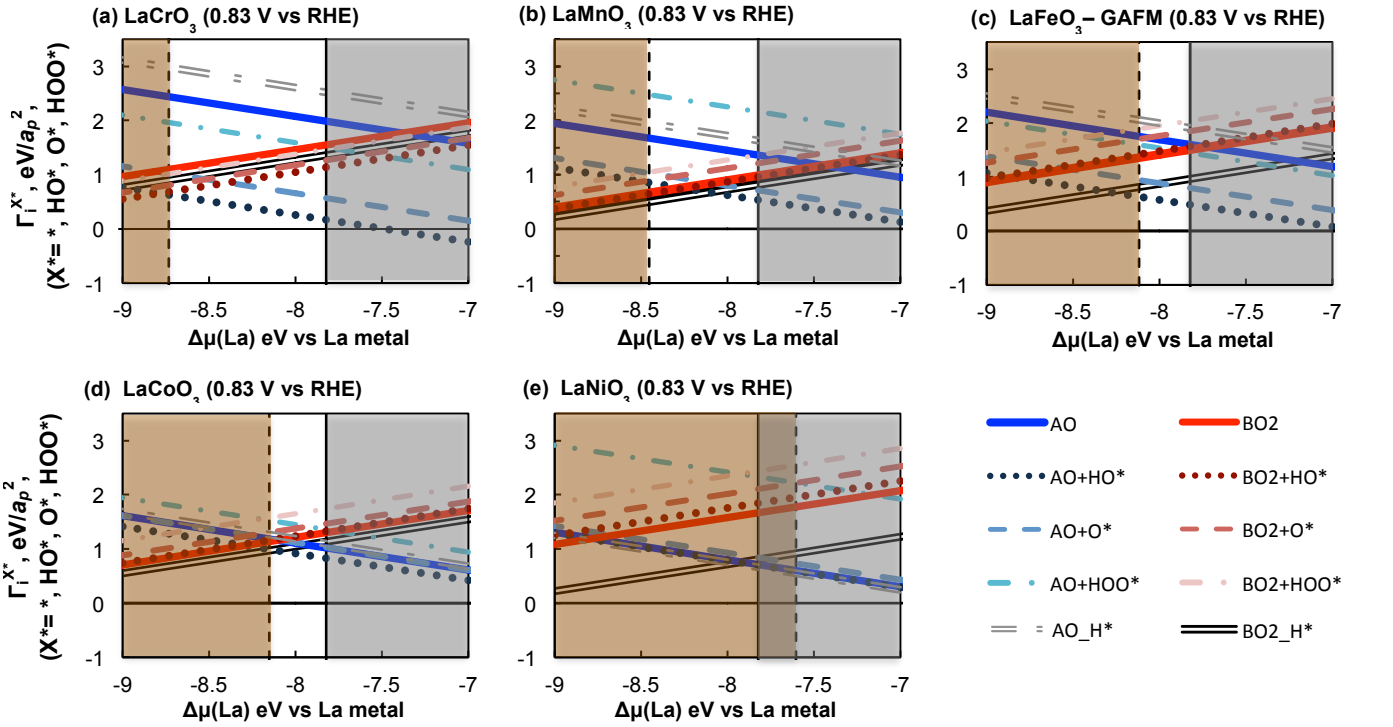

Figure 3. Stability of perovskite (001) AO and BO_2 surfaces with and without adsorbate coverage at applied potential of 0.83 V vs. RHE (SHE within the concerted proton-electron transfer scheme) as a function of La chemical potentials relative to the La metal (x-axis) for (a) $LaCrO_3$ (b) $LaMnO_3$ (c) $LaFeO_3$ (GAFM) (d) $LaCoO_3$ (e) $LaNiO_3$. The y-axis represents surface free energies per (1x1) (001) surface area, $\Gamma_i^{X^*}$ (eV/a_p^2 , where a_p is the bulk perovskite lattice constant) with and without adsorbate coverage. The bare surfaces without adsorbates, the surfaces with the stable coverage of HO*, the surfaces with the stable coverage of O*, the surfaces with the stable coverage of HOO*, and the surfaces with the stable coverage of H* are represented by thick solid lines, dotted lines, dashed lines, dotted dashed lines, and dotted dashed double lines, respectively, while the lines in red color (and in black color for H*) are for the perovskite (001) BO_2 surfaces while those in blue color (and in grey color for H*) are for the (001) AO surfaces. The two vertical lines in each plot indicate the conditions where the perovskite is in equilibrium with La_2O_3 (solid line) and in equilibrium with the most stable binary transition metal oxide compound at applied potential of 0.83 V vs. RHE as constructed in Figure 2. The grey (brown) shaded area indicates the region where perovskite is unstable relative to the La_2O_3 (the stable binary transition metal oxide). The unshaded area is the stable bulk perovskite region relative to both the La_2O_3 and the most stable binary transition metal oxide compound included in the stability analysis.

(green) surfaces of the $LaBO_3$ perovskites, and a summary of the (001) AO and BO_2 HO*, O*, HOO*, and H* surface adsorption coverage dependences is provided in Table 1. We note the calculated DFT adsorption energies, $\Delta\bar{E}$(X*) (X*= HO*, O*, HOO*, and H*), are only part of their free energies, $\Delta\bar{G}$(X*), as defined in Eqn. 7. Since the stable coverage of the adsorbates on the perovskite surfaces is dependent on the electrochemical conditions (*e.g.* the ($k_bTln(a_{H+})$- $e\phi$) term in Eqn. 1 and Eqn. 8), stability of the adsorbed species and the most stable coverage of adsorbates will also depend on the applied potentials for the perovskite (001) AO and BO_2 surfaces under the ORR and OER conditions, and will be further discussed below in Section C.3 and Section C.4.

Nonetheless, the relative adsorption energy difference between the two (001) AO and BO_2 surfaces does not depend on the electrochemical conditions and is intrinsically set by surface polarity of the surface terminations, due to opposite surface compensating charge originating from bulk polarity[26, 27] and different surface metal-oxygen bonding environments (metal-oxygen coordination). In general we found stronger binding energies on the (001) AO termination and weaker binding energies on the bare (001) BO_2 termination for HO*, O* and HOO*, with 0.6~4 eV differences between the two ideal (001) surfaces, as shown in Figure S1, Supporting Information. Such differences in the surface adsorption energies is intrinsic to surface termination types and independent of the external chemical condition or the chemical potential references. More detailed discussions on surface compensating charge occurring at the surfaces of polar transition metal perovskite systems are given in Ref. 27. Ref. 27 shows that extra surface charge doping can cause surface band bending and alter the O *2p*-band center position relative to the Fermi level, which results in distinct surface binding energy between the (001) AO and BO_2 surfaces. Qualitatively, the difference in binding energy can be understood from simple formal charge observations. The $A^{3+}O^{2-}$ surface is effectively reduced compared to the $B^{3+}(O^{2-})_2$ surface, which leads to stronger binding of oxidizing species (*e.g.*, O*) and weaker binding of reducing species (*e.g.*, H*) to AO compared to BO_2. Our results indicate that the HO*/O*/HOO* adsorption on the (001) surfaces of the investigated perovskites frequently exhibits weak coverage dependence, except for the (001) AO surface adsorption of $LaCrO_3$, $LaFeO_3$, and (to a lesser extent) $LaMnO_3$. Our results also show that H* adsorption on the (001) BO_2 surfaces generally exhibits strong coverage dependences. In addition, we find that H* is less stable on AO surfaces than on the BO_2 surfaces, and H* does not bind to this AO surface ($LaCrO_3$) or weakly bind ($LaMnO_3$ and $LaFeO_3$) at the condition close to the 0 V vs. RHE (the additional ΔZPE(H*)-$T\Delta S$(H*)+E_{solv}(H*) term for converting $\Delta\bar{E}$(H*) into $\Delta\bar{G}$(H*) at the 0 V vs. RHE is about +0.1 eV/H* and therefore the overall H* binding tendency at 0 V vs RHE can be approximated with the computed DFT adsorption energies relative to the H_2 gas phase).

3. Stability of the (001) AO and BO_2 surfaces with adsorbates under the ORR condition:

Following Eqn. 6, the stability of the perovskite surfaces at applied potential of 0.83 V vs. RHE with the HO*, O*, HOO* and H* adsorbates at various coverage between 0.25 ML and 1.0 ML were assessed by combining the surface free energies of the bare (001) AO and BO_2 surfaces with the calculated adsorption free energies, $\Delta\bar{G}$(X*) (per adsorbate), multiplied by their corresponding surface coverage, θ, per (1×1) surface area. In Figure S2, we showed the $\Delta\bar{G}$(X*)×θ's of each adsorbed species at the simulated coverage for the (001) AO (in red) and BO_2 (in green) surfaces. The lowest $\Delta\bar{G}$(X*)×θ in each plot represents the most stable coverage of the X* adsorbate, which correspond to the averaged surface adsorption energy per adsorbate. A summary of the most stable coverage for the (001) AO and BO_2 surfaces of $LaBO_3$ at applied potential of 0.83 V vs. RHE based on Figure S2 is provided in Table 2, where the most stable coverage of the adsorbates for the (001) AO and BO_2 surfaces of $LaBO_3$ at applied potential of 0.83 V vs. RHE based on Figure S2 is highlighted with bold font in a shaded background.

Table 2. The predicted stable coverage between 0.25 and 1.0 monolayer (ML) for each adsorbed species, HO*, O*, HOO*, and H*, on the perovskite (001) AO and BO_2 surfaces at 0.83V vs. RHE (close to the ORR condition), based on DFT energies and Eqn. 8. The most stable adsorbate covered surface among the four adsorbed species, based on the results of Figure S2, *i.e.* the lowest adsorption free energy multiplied by coverage ($\Delta\bar{G}$(X*)×θ), is labeled in bold font within grey shaded background.

$LaBO_3$ surfaces		HO*	O*	HOO*	H* (at surf. O)
$LaCrO_3$	(001) AO	**1.0**	0.5* (0.5~1.0)	0.5	0.25
	(001) BO_2	**1.0**	1.0	0.25	0.5
$LaMnO_3$	(001) AO	**1.0** (0.75, 1.0)	0.25	0.25	0.25
	(001) BO_2	0.25* (0.25, 0.5, 0.75, 1.0)	0.25	0.25	**0.5**
$LaFeO_3$ (GAFM)	(001) AO	**1.0**	0.5* (0.5,0.75)	0.25	0.25
	(001) BO_2	0.25	0.25	0.25	**0.5*** (0.5~0.75)
$LaCoO_3$	(001) AO	**0.5**	0.25	0.25	0.0
	(001) BO_2	0.25	0.25	0.25	**0.5**
$LaNiO_3$	(001) AO	0.25* (0.25, 0.5, 0.75, 1.0)	0.25	0.25	**0.25**
	(001) BO_2	0.25	0.25	0.25	**1.0**

In Figure 3 we show surface free energies of the bare (001) AO and BO_2 surfaces and the surfaces with stable coverage of each type of adsorbate (HO*, O*, HOO*, and H* as provided in Table 2) as a function of La chemical potential (relative to the La metal) at applied potential of 0.83 V vs. RHE close to the ORR conditions. The two vertical lines in each plot represent the La chemical potential conditions at which the perovskites are in equilibrium with La_2O_3 and the most stable MO_x at various oxidation states, and the shaded area indicates the region at which the bulk perovskite phase is stable relative to the La_2O_3 and MO_x[38-40]. Information regarding the most stable MO_x vs. the applied potential was also shown previously in Figure 2.

Generally we found that, close to the ORR condition, the (001) BO_2 surface is most stable with adsorbed H* (except $LaCrO_3$) and the (001) AO surface is most stable with adsorbed OH*. The stability of H* on $LaMnO_3$, $LaFeO_3$, $LaCoO_3$, and $LaNiO_3$, is in good agreement with the Mn, Fe, Co, and Ni Pourbaix

 This journal is © The Royal Society of Chemistry 2012

diagrams[43], where transition metals in these stable phases close to the ORR conditions (~0.8 V vs. RHE) are in the 3+ or less than 3+ oxidation state. The oxidation states of the transition metal cations at the (001) BO_2 surfaces are more than the 3+, due to the surface charge compensation to bulk polarity, and therefore the (001) BO_2 surfaces can be stabilized by adsorbing H* on surface oxygen to stabilize the transition metal minimize the surface energy. That the (001) BO_2 surface of Cr was shown in Figure 4 to be most stable with 1ML HO* coverage is also in good agreement with the Cr Pourbaix diagram where Cr^{3+} is stable at lower potential than 0.83V vs. RHE in alkaline solution (where CrO_4^{2-} is the stable phase at 0.83 V vs. RHE)[43]. The stability of HO* on the (001) AO surface is expected because of that positively charged nature of the $[LaO]^+$ surface termination (with additional electron doping due to polarity compensation) can be stabilized with HO^- adsorption (oxidation of the AO surfaces). Indeed, presence of the hydroxylated (001) AO surfaces was recently suggested by Stoerzinger *et al.*[53] on $LaCoO_3$ (001) film surfaces grown on Nb doped $SrTiO_3$ and on more general $LaBO_3$ (001) films (B=Cr, Mn, Fe, Co, and Ni)[24]. These trends are in good agreement with the predicated surface stability information shown in Figure 4, in which the stable HO* covered AO surfaces were predicted to be even more stable than the stable BO_2 surfaces or exhibited comparable stability to the BO_2 surfaces. Overall, our *ab initio* surface stability analysis suggested these surface coverage effects impact the stable surfaces, and therefore couple to the ORR/OER, as will be discussed below in Section D.4.

4. Stability of the (001) AO and BO_2 surfaces with adsorbates under the OER condition:

The same stability analysis for the perovskite (001) surfaces as described in Section C.3 was repeated at a typical OER applied potential of 1.63 V vs. RHE and the results are provided in Table 3 and Figure 4, which are parallel to Table 2 and Figure 3 calculated at the ORR potential. The most stable coverage of the adsorbates were determined based on Figure S3 and are highlighted in Table 3 with bold font and a shaded background.

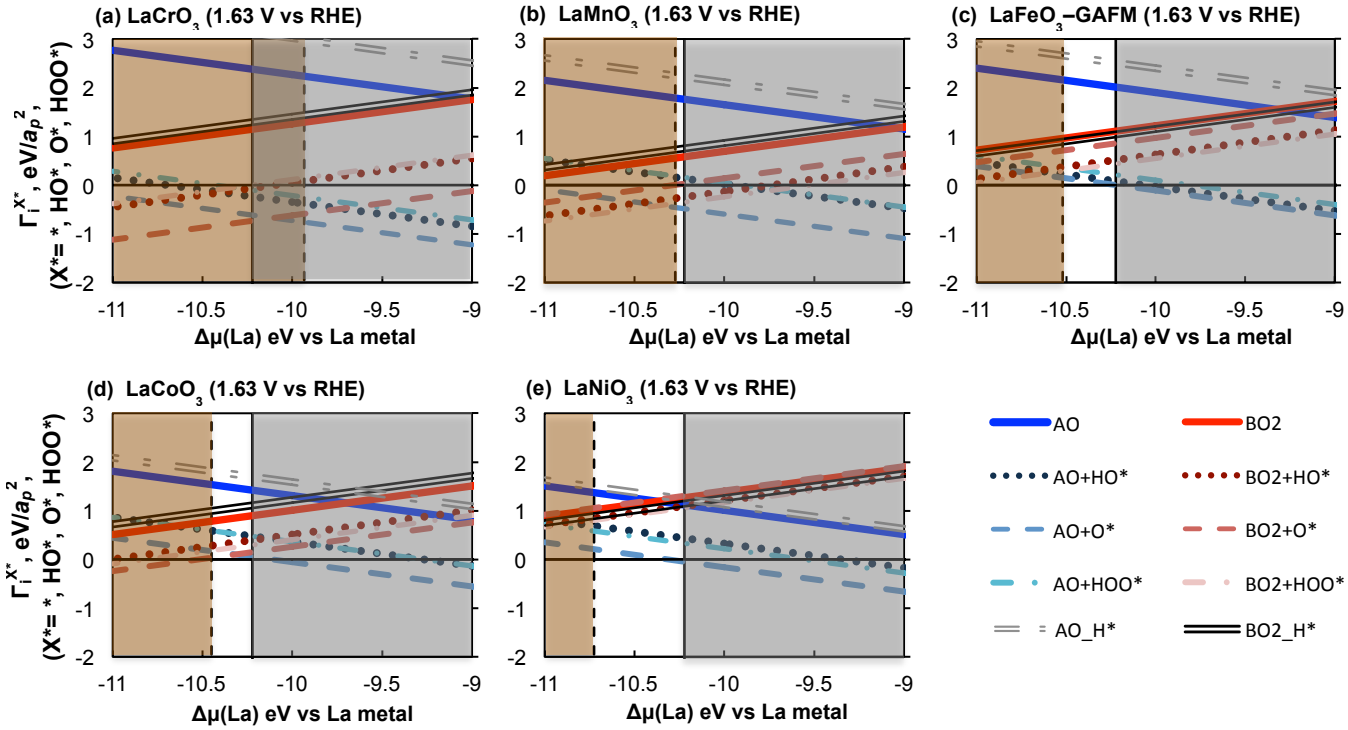

Figure 4. Stability of perovskite (001) AO and BO_2 surfaces with and without adsorbate coverage at applied potential of 1.63 V vs. RHE (SHE within the concerted proton-electron transfer scheme) as a function of La chemical potentials relative to the La metal (x-axis) for (a) $LaCrO_3$ (b) $LaMnO_3$ (c) $LaFeO_3$ (GAFM) (d) $LaCoO_3$ (e) $LaNiO_3$. The y-axis represents surface free energies per (1x1) (001) surface area, Γ_i^{X*} (eV/a_p^2, where a_p is the bulk perovskite lattice constant) with and without adsorbate coverage. The bare surfaces without adsorbates, the surfaces with the stable coverage of HO*, the surfaces with the stable coverage of O*, the surfaces with the stable coverage of HOO*, and the surfaces with the stable coverage of H* are represented by thick solid lines, dotted lines, dashed lines, dotted dashed lines, and dotted dashed double lines, respectively, while the lines in red color (and in black color for H*) are for the perovskite (001) BO_2 surfaces while those in blue color (and in grey color for H*) are for the (001) AO surfaces. The two vertical lines in each plot indicate the conditions where the perovskite is in equilibrium with La_2O_3 (solid line) and in equilibrium with the most stable binary transition metal oxide compound at applied potential of 1.63 V vs. RHE as constructed in Figure 2. The grey (brown) shaded area indicates the region where perovskite is unstable relative to the La_2O_3 (the stable binary transition metal oxide), while the brown shaded area indicates the region where perovskite is unstable relative to the the stable binary transition metal oxide. The unshaded area is the stable bulk perovskite region relative to both the La_2O_3 and the most stable binary transition metal oxide compound included in the stability analysis.

Table 3. The predicted stable coverage between 0.25 and 1.0 monolayer (ML) for each adsorbed species, HO*, O*, HOO*, and H*, on the perovskite (001) AO and BO_2 surfaces at 1.63V vs. RHE (close to the OER condition), based on DFT energies and Eqn. 8. The most stable adsorbate covered surface among the four adsorbed species, based on the results of Figure S3, *i.e.* the lowest adsorption free energy multiplied by coverage ($\Delta\bar{G}(X^*)\times\theta$), is labeled in bold font within grey shaded background.

$LaBO_3$ surfaces		HO*	O*	HOO*	H* (at surf. O)
$LaCrO_3$	(001) AO	1.0	**1.0**	1.0	0.25
	(001) BO_2	1.0	**1.0**	1.0	0.25
$LaMnO_3$	(001) AO		**1.0**	1.0	0.25
	(001) BO_2	1.0[a]	1.0	**1.0**[a]	0.25
$LaFeO_3$ (GAFM)	(001) AO	1.0	**0.75**[b] **(0.75, 1.0)**	1.0	0.25
	(001) BO_2	1.0[a]	1.0	**1.0**[a]	0.5
$LaCoO_3$	(001) AO	1.0	**1.0**	1.0	0.25
	(001) BO_2	1.0	**1.0**	1.0	0.25
$LaNiO_3$	(001) AO	1.0	**1.0**	1.0	0.25
	(001) BO_2	1.0[a]	0.25	**1.0**[a]	1.0[b] (0.5, 0.75, 1.0)

[a] the stability of HO* and HOO* at 1.63 V vs. RHE is close based on the scaling relationship.
[b] the stability of the stable coverage is close to the stability of those in the parenthesis (within 0.03 eV/a_p^2).

In contrast to the (001) surface stability results under the ORR condition shown previously in Figure 3, where the 1 ML HO* covered AO surface is the stable (001) surfaces for $LaCrO_3$ and $LaFeO_3$, the 1 ML adsorbate covered (001) BO_2 surfaces under the OER condition become stabilized and the surface energies are comparable to the 1 ML adsorbate covered AO surfaces for all the $LaBO_3$ except for $LaNiO_3$. The stabilization of the BO_2 (001) surfaces (with the stable adsorbates) under the OER condition, and the weak coverage dependent surface adsorption of the BO_2 surfaces shown in Figure S1, supports the use of the bare BO_2 surfaces for predicting OER activities of $LaBO_3$ located on the strong binding (near OER voltages) branch, as has been done in some previous studies[14]. However, our results also demonstrated that for systems such as $LaNiO_3$, whose OER activity was predicted to be high and close to the top of the OER volcano in the previous GGA study[14], the BO_2 surface was predicted to be less stable than the AO surfaces in our surface stability analysis. Therefore, the $LaNiO_3$ (001) AO surfaces must be considered in order to obtain the self-consistent OER activities at the stable surfaces.

It is also noted that in Figure 4 both the $LaCrO_3$ and $LaMnO_3$ (001) surfaces with 1 ML of stable adsorbates exhibit negative surface free energies under the OER condition, indicating the bulk phase is not stable relative to the stable adsorbate-covered surfaces, which is consistent with the bulk stability analysis. In fact, Bockris and Otagawa[54] suggested an intrinsic instability of Cr^{3+} on the surfaces of $LaCrO_3$ perovskites, where other lanthanum chromate with higher oxidation of Cr can form. As will be shown below, the instability of the bulk $LaCrO_3$ under the OER condition is consistent with the fact that a greater deviation between the predicted OER potential and the experimentally measured OER potential among the investigated perovskites was found for $LaCrO_3$. For $LaMnO_3$, the bulk stability analysis suggests the $LaMnO_3$ bulk phase can be close to the decomposition limit with respect to La_2O_3 and MnO_2 under the OER condition. However, it is well known that stabilization of the $LaMnO_3$ bulk can occur through formation of cation vacancies in air at high temperature[55, 56] and therefore the stable bulk $LaMnO_3$ and its surfaces under the OER condition are likely to contain significant content of cation vacancies. Indeed, a very recent DFT study by Rong *et al.*[57] investigated stability of the $LaMnO_3$ (001) surfaces with various surface reconstructions using the standard GGA method. The calculated surface phase diagram indicated instability of the $LaMnO_3$ (001) BO_2 surfaces upon increasing applied voltage and under the OER condition (close to 1.63 V vs. RHE) the (001) BO_2 surfaces contained Mn vacancies, which was then attributed to causing a similar surface Mn oxidation state between $LaMnO_3$ vs. $LaMnO_{3+\delta}$ and consequently their similar OER activities as found in the experimental measurement[4]. Nonetheless, since the bulk defect chemistry and oxygen nonstoichiometry of $LaMnO_{3\pm\delta}$ at a wide range of temperature and oxygen partial pressure has been shown to be well described by the GGA+U apporach[56], further *ab initio* thermodynamic modeling including treatment of electron correlation error in GGA as well as formation of cation vacancies in the bulk and on the surfaces under the OER condition is needed to refine the surface stability with respect to the stable bulk $LaMnO_{3+\delta}$.

Focusing on $LaNiO_3$ (001) surface stability under the OER condition as shown in Figure 4(e), the (001) AO surfaces was revealed to exhibit greater stability than the stable adsorbate covered BO_2 surfaces, which is consistent with $LaNiO_3$ having the highest tendency to be reduced among the investigated perovskites. Overall, the surface stability results indicate that under the OER conditions, both the (001) AO and BO_2 surfaces of the investigated $LaBO_3$ perovskites in general are covered with the O* or HO*/HOO* adsorbates at high or full coverage.

In the following section, we will distinguish the perovskite (001) bare surfaces with weak coverage dependent surface adsorption from those exhibiting strong/moderate coverage dependences (*i.e.* $LaCrO_3$, $LaFeO_3$, and $LaMnO_3$ (001) AO surfaces) and the cases of the surfaces being stabilized with H* coverage (mainly under the ORR conditions for the BO_2 surfaces). The theoretical OER and ORR volcanoes were first constructed based on surface adsorption free energies of the OER/ORR reaction intermediates simulated at low coverage for the surfaces that exhibit weak coverage dependences. Then, the most stable surface coverage from the surface stability analysis was incorporated to self-consistently predict the ORR activities for systems with strong/moderate coverage dependences or being stabilized with H* coverage under the operating conditions.

D. Results- Predicted ORR and OER Activities

In this section, the framework of the thermodynamic overpotential methods[14, 16, 28] was utilized to construct the ORR/OER volcanoes and predict the ORR/OER activities of the $LaBO_3$ perovskite (001) AO and BO_2 surfaces. We first focused on surface adsorption energies for the HO*, O*, and HOO* reaction intermediates at the bare surfaces that exhibit weak coverage dependence (as summarized in Table 1) as these are simpler to consider than the surfaces with strong coverage dependence. We first made a direct comparison of results calculated at the GGA+U level with the results calculated at the GGA level[14], for assessment of the effect of including Hubbard

 This journal is © The Royal Society of Chemistry 2012

U corrections on the surface adsorption energies and their scaling relationship, as well as the predicted ORR/OER activities. In addition, we examined the trends between the adsorption energies and the electronic structure descriptors, *i.e., d*-electron filling of the transition metals[1, 8] as well as the O *2p*-band center relative the Fermi level[58]. We revealed that an excellent correlation exists between the sub-surface layer O *2p*-band center and the computed (001) AO and BO_2 bare surface HO* adsorption energies, which can be attributed to shifts of surface electron energy level near the surfaces due to compensating surface charge from bulk polarity (*i.e.* surface band bending effect). We showed the universal scaling relationship between ΔE(HOO*) and ΔE(HO*) held for both the (001) AO and BO_2 surfaces as well as the (110) surfaces calculated with the GGA+U method (which also suggests a correlation between the sub-surface layer O *2p*-band center and the HOO* adsorption energies). However, there existed a poorer correlation of ΔE(O*) vs. ΔE(HO*) due to the distinct bonding nature between M-O* (multiple bond) and M-OH*, where the treatment *d*-electron correlation upon inclusion of the Hubbard U correction in DFT leads to larger variation of ΔE(O*) vs. ΔE(HO*), in agreement with a less clear trend of transition metal-oxo bond strength vs. the transition metal Mn~Ni series reported in the literature. In addition, the predicted stable coverage of the perovskite surfaces shown in Section C were further included to assess their influences on the predicted OER/ORR activities relative to those of the bare surfaces. Our results indicated that the coverage effect can lead to a significant change in the predicted activities of the (001) AO surfaces.

1. Surface adsorption energies and the scaling relationship for bare surfaces:

The scaling relationships of our GGA+U adsorption energies of ΔE(HO*), ΔE(O*), and ΔE(HOO*) vs. ΔE(HO*) calculated at the ¼ ML coverage are presented in Figure 5(a), along with the RPBE results taken from Ref. 14 shown in Figure 5(b). Comparing the adsorption energy results shown Figure 5(a) and Figure 5(b), a weakening of adsorption energies of the transition metal perovskites upon including Hubbard U_{eff} is observed. This weakening is consistent with the work of Garcia-Mota *et al*.[22] and was also revealed in our previous work[34], where surface adsorption energies upon inclusion of Hubbard U correction has been shown to correlate with shift downward of O *2p*-band center relative to the Fermi level (Figure S2 of Ref. [58]). An further weakening effect for hybrid functionals was shown by Wang *et al*.[15] for ΔE(HO*), ΔE(O*), and ΔE(HOO*) adsorption energies by comparing the hybrid functional results to those calculated with the GGA+U approach. Wang *et al*. generally found a shift of +0.2 to +0.4 eV, and a particularly shift of +0.8 eV for $LaFeO_3$ ΔE(HOO*)). These hybrid functional and GGA+U results suggest that either including the Hubbard U_{eff} correction or using the hybrid functional method to treat correlated electron errors in DFT-GGA for transition metal oxides will make transition metal oxides less oxyphilic[19, 59], and therefore result in reduction of surface oxygen adsorption strength. This result is due to the same physics shown in studies of battery electrode Li intercalation and associated transition metal redox energies, where adding U and using hybrid methods when compared to plain DFT increases predicted Li voltages, consistent with a increase in electronegativity, which is expected to correlated with a decrease in oxyphilicity[59, 60]. These trends have been associated with the correction of self-interaction terms with the DFT+U, making oxidation harder and reduction easier.[60]

Although inclusion of the Hubbard U_{eff} correction weakens the ΔE(HO*), ΔE(O*), and ΔE(HOO*) in our GGA+U results, the scaling relationship of ΔE(HOO*) vs. ΔE(HO*) calculated at low coverage is still sustained, which leads to the same optimal binding strength in the OER/ORR volcano plot as seen in those calculated at the GGA level (RBPE) [14, 61]. The expression of the scaling relationship was suggested to be in the following form [14]:

$$\Delta E(HOO^*) = \Delta E(HO^*) + 3.2\ (\pm 0.2)\ eV \qquad \text{Eqn. 9}$$

We have performed additional assessment of adsorption energies of HO*, O*, and HOO* on the bare (001) AO and BO_2 and (110) ABO surfaces for $LaCrO_3$ and $LaMnO_3$, which again confirms such scaling relations, as shown in Figure S5, Supporting Information. The physical origin of such linear scaling relationship has been explained by Rossmeisl *et al.* based on the same single bonding nature of HO* and HOO* [16] and the 3.4 eV difference in the OH^- and HO_2^- and in aqueous solution[29].

2. Surface HO* adsorption energies vs. electronic structure descriptors:

In the following discussions, we examined the trends of surface HO* adsorption energies vs. selected first principles based electronic structure descriptors, including *d*-electron filling of the transition metals[1, 8] as well as the O *2p*-band center relative the Fermi level[58].

Comparing the trends in the HO* adsorption strength for the $LaBO_3$ (B=Cr, Mn, Fe, Co, and Ni) series between the GGA+U and the RPBE[14], the GGA+U results are in the following order for the (001) BO_2 bare surfaces (systems with more negative values of adsorption energy have stronger surface binding are listed first): Cr(FM), Fe(FM), Mn(FM), Co(FM), Fe(GAFM), and Ni(FM) while the trend of the HO* adsorption energy calculated with RPBE follows the *d*-electron filling, *i.e.,* Cr, Mn, Fe, Co, and Ni[8, 14]. However, some discrepancy between the *d*-band filling order and the binding strength order exists for Fe in the GGA+U calculations. In particular, compared to the order of *d*-electron filling, Fe(FM) binds more stronger than expected, and switches order to before Mn, while Fe(GAFM) binds more weakly, and switches order to after Co. As will be discussed below, distinct electronic structures between the G-type AFM and FM state of the Fe may be responsible for such discrepancy. We note that in this work we used the ground state G-type AFM to represent the $LaFeO_3$ system while in general also included the FM-state $LaFeO_3$ results. We did not attempt to resolve the surface magnetic states for surface adsorption properties between FM and G-type AFM under the ORR/OER conditions, whose values will influence the predictions for the $LaFeO_3$ system and may be necessary to determine for accurate comparisons to experiments. Overall, for the bare (001) BO_2 termination, the trend of surface adsorption strength among different $LaBO_3$ systems can be fairly well described by their *d*-electron filling, with increased filling corresponding to weaker binding, except that additional complexity arises in the surface HO* adsorption strength between two different magnetic ordering (G-tyep AFM vs. FM) in $LaFeO_3$. This trend is what is expected from standard *d*-band theory, where higher *d*-electron

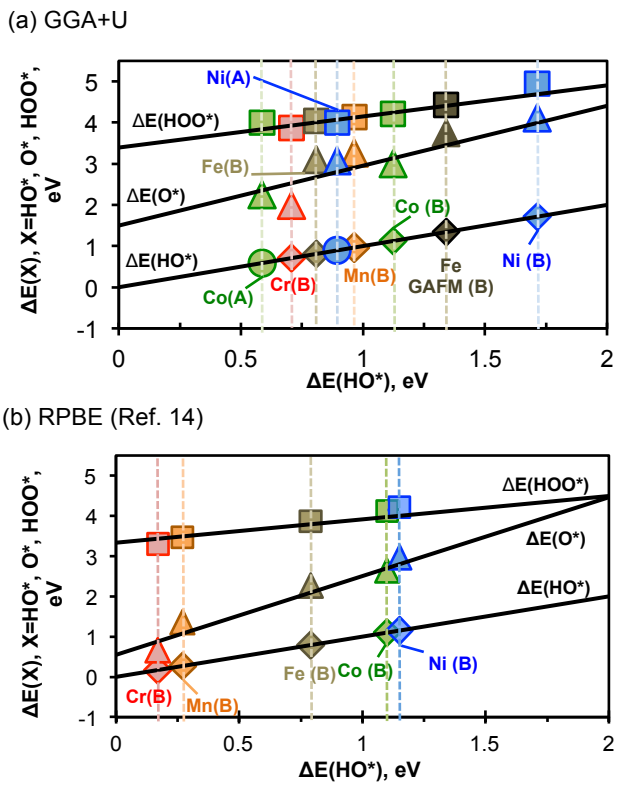

Figure 5. (a) The scaling relations of ΔE(X), X=HO* (circles for the (001) AO surfaces and diamonds for the (001) BO_2 surfaces), O* (triangles), HOO* (squares) for the $LaBO_3$ (B=Cr, Mn, Fe, Co, and Ni) perovskite (001) surfaces calculated with (a) GGA+U with U_{eff} for the *d*-electrons of transition metal elements from Ref. 19. All calculations were performed based on the adsorption configuration of the (001) BO_2 and AO bare surfaces using the H_2O/H_2 energy reference[14, 28]. The light olive symbols represent the ferromagnetic states while the dark olive symbols represent the G-type AFM $LaFeO_3$. The G-type AFM is included additionally for $LaFeO_3$ due to the high Neél temperature (T_N=740 K[36]), while T_N of the other perovskite systems are below the room temperature[36] and are modeled using the ferromagnetic state in order to have a set of consistent and tractable magnetic arrangement. (b) The RPBE results taken from Ref. 14.

filling leads to weaker the adsorption strength due to increased filling of the antibonding states[62].

In addition to the *d*-band filling, our previous work has demonstrated that the perovskite bulk and (001) BO_2 surface O *2p*-band centers also correlate with the (001) BO_2 surface O* binding energies[58]. In the following discussion, we further elaborated how O *2p*-band centers can be utilized to provide unified description on the distinct surface HO* adsorption strength between the two (001) AO and BO_2 bare surfaces of the investigated $LaBO_3$ systems, by considering the surface band bending effect and distinct local symmetry of surface oxygens between the two (001) surface terminations.

Since the top (001) AO surface layer contains under-coordinated oxygen with only one transition metal-oxygen (TM-O) bond whereas both oxygens in the (001) BO_2 surface layer and in bulk contain two TM-O bonds, the oxygens of the (001) AO surface termination show distinct O *2p*-band

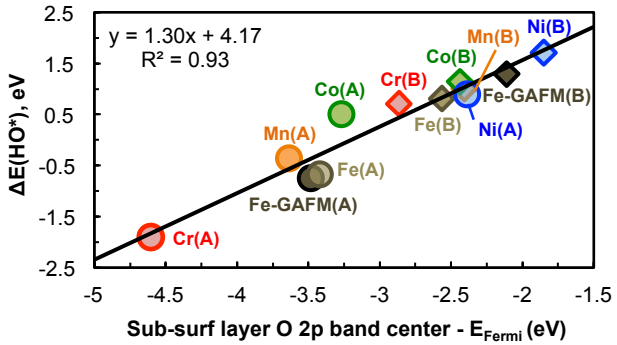

Figure 6. The calculated ΔE(HO*) of the $LaBO_3$ (001) BO_2 and AO bare surfaces vs. the sub-surface layer O *2p*-band center (the second slab layer beneath the surface termination), where the good linear correlation with R^2=0.93 in the plot suggests effectiveness of using the sub-surface O *2p*-band center to describe the surface HO* adsorption strength.

character from the other oxygen in the slab, as shown in Figure S4, Supporting Information. Therefore, in this work we utilized the sub-surface layer (layer beneath the surface layer) fully coordinated oxygen for calculating the O *2p*-band centers to correlate with the surface adsorption energies. We use this subsurface layer for both the AO and BO_2 surfaces for consistency. In Figure 6, we show the calculated sub-surface layer (the layer beneath the surface layer) O *2p*-band center vs. the calculated Δ E(HO*)s of the $LaBO_3$ (001) AO and BO_2 surfaces (B=Cr, Mn, Fe, Co and Ni). A linear correlation between the calculated sub-surface layer O *2p*-band center vs. the Δ E(HO*)s suggests the effectiveness of the sub-surface layer O *2p*-band center in describing the surface binding energies of both the AO and BO_2 terminations for the investigated perovskite systems, as shown in Figure 6. The O *2p*-band center is generally useful to capture the energetics of oxygen as it describes where the oxygen electrons will reside in the solid. Our use of the subsurface layer O, as opposed to the bulk O, captures the O *2p*-band center shift (relative to the Fermi level of the slab) due to the band bending near the surface region, which is most relevant for metal oxygen bond-strength near the surfaces and further correlates with the surface adsorption energies. With an approximation of aligning the Fermi level of the slab models with the bulk for the close-to-metallic systems such as $LaCoO_3$ and $LaNiO_3$, one can compare the sub-surface layer O *2p*-band centers of the (001) AO and BO_2 slab models with the calculated bulk O 2p band center of $LaCoO_3$ (~ -2.6 eV relative to the Fermi level) and $LaNiO_3$ (~ -2.0 eV relative to the Fermi level) reported in Ref. [58], as shown in Figure S6, Supporting Information. The higher O *2p*-band center of the sub-surface layer beneath the BO_2 surface (the lower O *2p*-band center of the sub-surface layer beneath the AO surface) vs. their bulk O *2p*-band centers (all relative to the Fermi level) suggests band bending up near the BO_2 surface and band bending down near the AO surface. Therefore, the distinct sub-surface layer O *2p*- band position of the (001) AO vs. BO_2 slabs relative to that of the bulk is consistent with the surface band bending picture due to surface charge compensation originated from the bulk polarity of the III-III perovskite[26], where extra electrons are introduced the (001) AO surfaces and extra hole are introduced to the BO_2 surfaces, creating an electric field near the bare (001) surfaces[27].

This journal is © The Royal Society of Chemistry 2012

We note a general trend of stronger (001) AO surface binding vs. weaker (001) BO_2 surface binding in each of the $LaBO_3$ systems, this trend being associated with the opposite surface band bending between the (001) AO and BO_2 terminations[27]. We note that this trend is note well captured by *d*-band filling. The electron doped AO surface termination exhibits a higher filling of the *d*-electron energy level than the (hole doped) BO_2 surface, whereas the HO* binding strength is stronger on the AO surface than the BO_2 surface. Thus we are finding that when comparing AO and BO2 surfaces the binding decreases with *d*-band, which is opposite the correlation noted above for BO_2 surfaces and different B cations. Recently, Calle-Vallejo proposed that the number of the outer *d*-electrons (*i.e.*, the *d*-valence electrons that are remaining on the metal atom upon oxidation) as an binding energy descriptor for perovskite oxides[63], which better describes the trend of surface binding between the AO vs. BO_2 surfaces than just the *d*-band filling, as there is more electron doping near the AO surfaces vs. more hole doping near the BO_2 surfaces. Nonetheless, assigning the number of total or outer *d*-electrons for a particular surface termination is not as straightforward as the bulk, and therefore use of the sub-surface layer O *2p*-band centers relative to the Fermi level provides a more robust and consistent description on adsorption strength of different surface terminations among the investigated $LaBO_3$ (Figure 6). Furthermore, as has been highlighted previously, additional complexity may arise in the case of Fe, where different magnetic coupling within the same number of outer *d*-electrons can results in distinct adsorption properties, as shown in Figure 5(a). The distinct $LaFeO_3$ surface adsorption between the G-type AFM and FM magnetic configuration were also found to correlate with their O *2p*-band centers near the surfaces, where the ground state G-type AFM $LaFeO_3$ contains a higher O *2p*-band center relative to the Fermi level than that of the FM $LaFeO_3$, which was in accordance the weaker surface binding energies (by +0.5~0.7 eV for ΔG(HO*), ΔG(O*) and ΔG(HOO*)) of G-type AFM $LaFeO_3$ than that of FM $LaFeO_3$ BO surface. More detailed discussions on the magnetic ordering effect for $LaFeO_3$ (001) surface adsorption properties, including both the AO and BO_2 surfaces, will be addressed in Section D.4.3 below. Here, we mainly highlight the effectiveness and robustness of the (sub-) surface layer O *2p*-band center in correlating with the surface adsorption properties between the two (001) terminations among the investigated $LaBO_3$ systems, as well as the capability of distinguishing different adsorption strengths for the $LaFeO_3$ perovskite (001) BO_2 surfaces with different magnetic ordering

3. Construction of Theoretical OER and ORR Volcanoes – bare surfaces

The adsorption free energy of OER/ORR reaction intermediates at the bare surfaces can be used for construction of theoretical OER/ORR volcanoes when the surfaces exhibit weak coverage dependence. In such a scenario, both the ORR and OER activity volcanoes can be presented in the same volcano plot, following the four OER/ORR charge transferring steps and using the scaling relationships between surface reaction free energies and a surface binding energy descriptor[16, 28]. Here we first consider the descriptor used by Man, *et al*, ΔG(O*) - ΔG(HO*)[14]. Unfortunately, a large scattering of ΔE(O*) leads to a poorer correlation between ΔE(O*) and ΔE(HO*), and therefore using a single surface binding energy descriptor to construct theoretical OER and ORR volcanoes using the GGA+U method

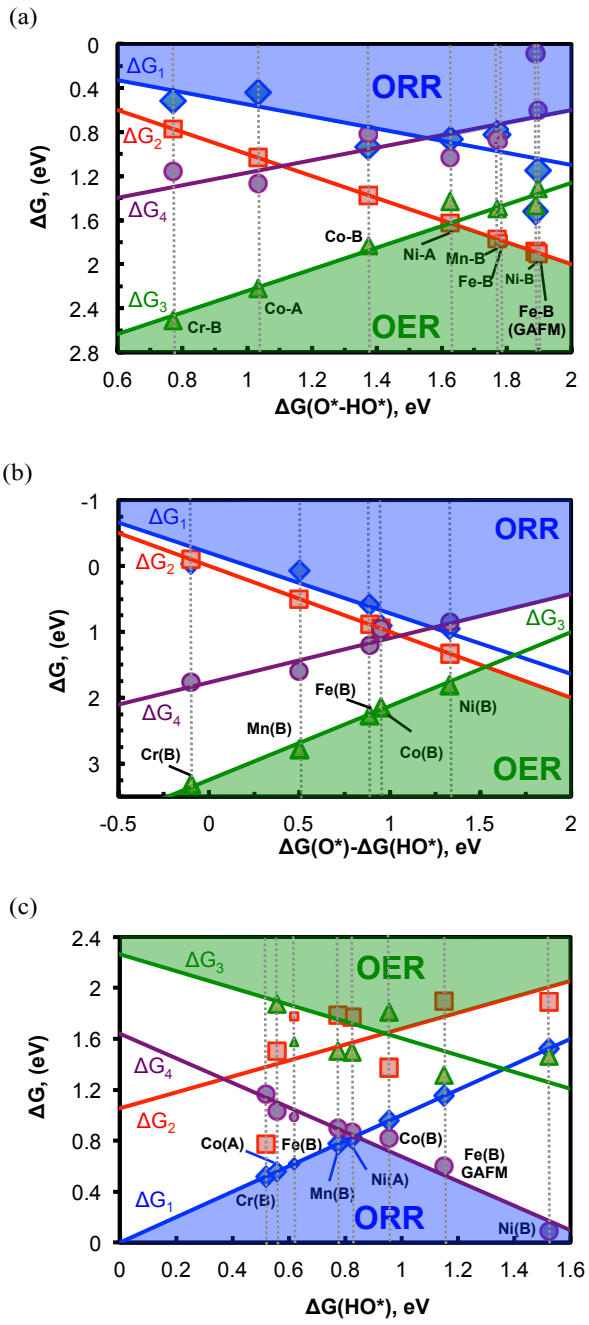

Figure 7. Calculated ΔG_1 ($H_2O(l)$ + * ⇆ HO* + H^+ + e^-), ΔG_2 (HO* ⇆ O* + H^+ + e^-), ΔG_3 (O* + $H_2O(l)$ ⇆ HOO* + H^+ + e^-), and ΔG_4 (HOO* ⇆ $O_2(g)$ + H^+ + e^-) vs. (a) ΔG(O*-HO*), calculated using the GGA+U method with U_{eff}s for the *d*-electrons transition metal elements from Ref. 19, for showing the OER volcano (b) ΔG(O*-HO*) of RPBE (data from Ref. 14) for showing both the OER (lower part) and ORR (upper part) volcano, (c) ΔG(HO*) calculated using the GGA+U method, for showing the ORR volcano, due to large scattering of ΔE(O*) in visualizing the ORR trend in Figure 7(a). All the free energy calculations are based on the DFT ΔE(HO*), ΔE(O*), and ΔE(HOO*) energies shown in Figure 5, with the zero point energy and entropy corrections taken from the tabulated terms in Refs. 14, 16, 28, and the solvation free energy corrections for HO*, O* and HOO* from Ref. 46.

does not to allow one to robustly distinguish both OER and ORR activity trends within the same volcano plot, as can be seen in the upper part of Figure 7(a). To better visualize the trend, ΔG(O*) - ΔG(HO*) was used as the OER activity descriptor for the theoretical OER activity volcano plot, as shown in Figure 7(a) and (b), while ΔG(HO*) was used as the ORR activity descriptor for the theoretical ORR activity volcano plot, as shown in Figure 7(c). As can be seen from these figures, the linear correlations controlling the OER region in Figure 7(b) and ORR region in Figure 7(c) are quite robust, making the described regions also robust.

We find that the scatter of ΔE(O*) vs. ΔE(HO*) from a linear correlation is enhanced in our GGA+U results as compared to those calculated at the GGA level[14], although deviation from the ΔE(O*) vs. ΔE(HO*) correlation also exists for a few perovskites calculated at the GGA level, as reported first in the RPBE results from Man *et al*[14]. The physical origin of scatter in the ΔE(O*) vs. ΔE(HO*) correlation may be understood by noting the formation of doubly bonded surface terminal M-O* species (*i.e.* surface adsorbed O*) and improved description on the electronic structures and energetics[22, 64] in the GGA+U calculations. We believe that the M-O* species are doubly with the GGA+U method) are very comparable to the M-O bond length of transition metal-oxo complexes (1.6~1.7 Å)[65] except for $LaNiO_3$. Since it has been shown that there is no clear correlation in the metal-oxo stability among Mn, Fe, and Co[66], which was explained by the electronic structure of the transition metal-oxo multiple bonding (include both σ and π bonds)[67], it is reasonable to suppose that the improved description on the electronic structures and energetics of transition metal oxides with inclusion of the Hubbard U correction can also lead to reduced correlation between the ΔE(O*) vs. ΔE(HO*) binding energies for the investigated $LaBO_3$ (M = Cr, Mn, Fe, Co, and Ni) as compared to the GGA predictions[14].

4. Theoretical vs. experimental ORR and OER potentials – bare surfaces

4.1 Theoretical vs. experimental OER potentials for bare surfaces with weak coverage dependent adsorption properties

Due to their weak coverage dependent surface adsorption properties, stabilization of the (001) BO_2 surfaces with their stable coverage relative to the (stable) AO surfaces under the OER conditions allows us to focus on the BO_2 surfaces with more simplified DFT modeling. In Figure 8 we plot the theoretically predicted OER voltages of the investigated perovskites in this work calculated with the GGA+U method (excluding the $LaCrO_3$, $LaFeO_3$, and $LaMnO_3$ (001) AO surfaces that exhibit strong or moderate coverage dependence) and the RPBE results reported by Man *et al.*[14]. All energies are based on bare surface calculations (which is a good approximation for these weak coverage dependent adsorption surfaces) and include all the surfaces that are stable under the OER conditions (see Figure 4). We note that while the experimental measurements were performed using catalyst ink prepared by mixing perovskite oxide powders and acetylene black carbon where multiple surface terminations may exist as well as the carbon mixture was not explicitly included in our theoretical model, we believe that our detailed investigations on the $LaBO_3$ perovskite (001) AO and BO_2 surfaces, which were intrinsically distinct based on their opposite surface charge compensation, as well as the various surface-adsorbate

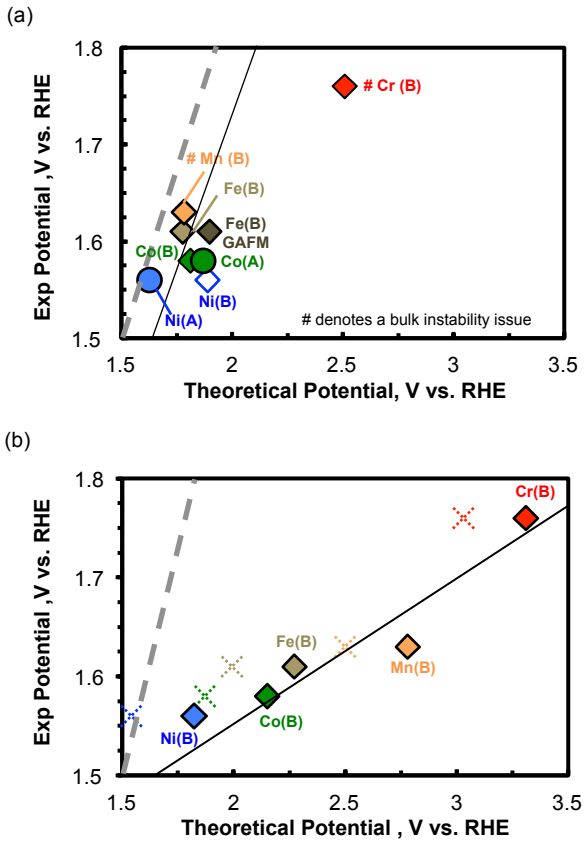

Figure 8. Experimental OER potentials (measured using catalyst ink prepared by mixing perovskite oxide powders and acetylene black carbon with tetrahydrofuran and an appropriate amount of neutralized Nafion)[4, 68] vs. theoretical OER potentials on perovskite $LaBO_3$ (B=Cr, Mn, Fe (GAFM and FM), Co, and Ni) bare (001) surface calculated with (a) GGA+U with U_{eff}s for *d*-electrons of transition metal elements from Ref. 19. For simplicity, only transition elements are labelled to represent the perovskite systems. A and B in parenthesis indicate the predicted ORR potentials on the (001) bare AO and BO_2 surface termination, respectively. All the perovskites (001) slabs are modelled using the ferromagnetic state, and an additional G-type AFM (001) BO_2 slabs are included for $LaFeO_3$, due to the high T_N (= ~740 K) of the $LaFeO_3$ system. The predicted OER potentials are obtained based on the reaction free energies volcano plot shown in Figure 5(a). Taking into account the weak coverage dependence in the surface adsorption (summarized in Table 1) and the surface stability analysis results shown in Figure 5, the solid symbols in Figure 7(a) represent the OER activities of the (001) stable surfaces, while the empty symbol for $LaNiO_3$ indicates the predicted OER activity of the less stable (001) BO_2 surfaces. The dashed lines represent the best fit to the experimental results and the thin solid lines are only for the purpose of guidance. (b) RPBE predictions (data from Ref. 14), where the solid symbols contain additional solvation free energy correction terms for adsorbed HO*, O*, and HOO* from Ref. 46 while the cross symbols represent the RPEB results without the solvation free energy corrections (*i.e.* corresponds to the predicted OER potentials in Ref. 14).

interactions including both the oxidizing (HO*/O*/HOO*) and reducing (H*) adsorbates at different coverage, provide a more robust thermodynamic constraint through exploration of a wider range of the phase space for quantitative descriptions on

 This journal is © The Royal Society of Chemistry 2012

oxygen electrocatalytic activities among the various $LaBO_3$ perovskites. Further experimental characterizations and measurements on the well-defined (001) surfaces of the perovskites will be of greater relevance and importance for direct comparisons between the theoretically predicted stable (001) surface coverage and OER/ORR activities to resolve the key fundamental limitations in understanding surface structure–function relationships between the electrocatalytic activity and the atomic-level surface structure.

For the OER predictions, we show both our GGA+U results and those obtained based on the GGA-RPBE energies reported in Ref. 14. It is seen that the RPBE results give a better linear correlation between the theoretical vs. experimentally measured OER potentials, although large differences in the values are clearly seen in Figure 8(b). In contrast, our GGA+U results improve the mean absolute error as compared to the experiments, while the scattering of the data in the linear correlation is enhanced. However, this decreased linear correlation is at least in part due to closer agreement of the predictions with the narrow experimental OER potential window (only about 0.3 V), which makes getting the correct order more challenging than when the values are spread over a greater range. Inspecting the optimal OER catalyst among the investigated perovskites, our results are in agreement with Man *et al.*[14] that $LaNiO_3$ is predicted to be the most active, although our prediction indicates that this is true only for AO terminated surface, which was not the one studied by Man *et al.*. We predict that the (001) BO_2 surface is significantly less active than the AO surface. The weakening of surface adsorption energies with inclusion of the Hubbard U_{eff} correction shifts the $LaNiO_3$ (001) BO_2 surface OER activity from the top of the volcano calculated with RPBE [14] to the weak binding branch of the volcano in our GGA+U calculations. On the other hand, with inclusion of the Hubbard U_{eff} correction, the (001) AO surfaces become more active than the (001) BO_2 surfaces. The predicted GGA+U OER potential for $LaCrO_3$ (001) (BO_2) surfaces in Figure 8(a) shows by far the largest deviation from the experimental OER potential among the investigated perovskites, as discussed previously in Section C.4. A further assessment by explicitly including the stable coverage of 0.75 ML O* as surface adsorbed spectator species at 1.63V vs. RHE does not significantly improve on the predicted OER potential (2.26 V for the 0.75 ML O* vs. 2.51 V predicted at the bare (001) BO_2 surface), consistent with the weak coverage dependence of the $LaCrO_3$ (001) BO_2 surface adsorption energy results shown in Figure S1. Such deviation between the theoretically predicted vs. experimentally measured $LaCrO_3$ OER potentials may be attributed to the $LaCrO_3$ instability. As shown in Figure 2, our bulk stability analysis suggests that $LaCrO_3$ is unstable relative to Cr binary oxides under the OER conditions. In addition, the surface stability analysis results shown in Figure 4, where the (001) AO and BO_2 surfaces covered with the adsorbates are more stable than the bulk, also suggests a tendency to form Cr compounds/species at higher oxidation states. Therefore, we believe that the true Cr system forms compounds other than LaCrO3 and therefore our model cannot predict the activity of this system. However, we note that if the surface follows our predicted tendency to form Cr compounds/species at higher oxidation states the surface adsorption energies are likely to be weakened and the potential shifted toward to the experimentally measured OER potential. Therefore, although we cannot successfully model $LaCrO_3$ with the approaches taken here, our results demonstrate its instability, explain its anomalous behavior, and suggest that the stable structures would have binding more consistent with the measure values.

4.2 Theoretical vs. experimental ORR potentials for bare surfaces with weak coverage dependent adsorption properties

Figure 9 shows the predicted GGA+U ORR potentials (Figure 9(a)) for the bare surfaces that exhibit weak coverage dependent surface adsorption properties for HO*, O*, and HOO*, in comparison with the predictions using the RBPE energetics reported in Ref. 14 (Figure 9(b)). While the stable (001) BO_2 surfaces of the investigated perovskites were predicted to be covered or partially covered with H*, which can lead to change of the HO* adsorption energies vs. those simulated at the bare surfaces, such effects were found to be mainly causing changes of ΔE(HO*) within ~0.3 eV for the predicted stable surfaces which will be further discussed below in Section D.5 (the $LaNiO_3$-(001) BO_2 surface is an exceptional case, where a much greater H* affinity causes a more enhanced stabilization of HO* adsorption by 0.4 eV at 1ML H* coverage). Therefore the predicted ORR potentials based on the bare surfaces with weak coverage dependent HO*, O*, and HOO* surface adsorption are a reasonable approximation (within 0.3-0.4 eV) to our best model for the ORR and can serve to give qualitative guidance without the complexity of including complex surface coverages, except for $LaNiO_3$. In particular, the calculations provide direct evidence of how important it is to include the Hubbard U_{eff} correction for predicting the ORR potentials on the perovskite surfaces, since a much better agreement with the experimental ORR potentials[5] is found for our GGA+U simulations than those simulations done with the RPBE method. Such improvement in modeling the ORR activities of the $LaBO_3$ perovskites upon inclusion of the Hubbard U_{eff} suggest the error in treating correlated electrons in transition metal perovskites calculated at the GGA level indeed has to be fixed in order to achieve the correct ORR activity trend. Nonetheless, the surface stability analysis revealed greater stability of the 1ML HO* covered AO surfaces of $LaCrO_3$ and $LaFeO_3$ than their stable BO_2 surfaces under the ORR condition (Figure 3). Therefore an additional assessment to include the stable AO surfaces with 1ML HO* coverage is needed in order to reach thermodynamic self-consistency for the predicted ORR activities on the (001) surfaces of the $LaBO_3$ perovskites, which will also be discussed below in Section D.5.

4.3 Influence of the magnetic ordering on OER and ORR activities for the $LaFeO_3$ (001) surfaces

While $LaFeO_3$ exhibit different (001) BO_2 surface adsorption strength due to the different magnetic ordering as discussed previously (*i.e.* strong adsorption strength for the FM vs. weak adsorption strength for the G-type AFM), the predicted OER are found to be comparable. For OER, the rate limiting reactions are predicted to be ΔG_2 (HO* ⇆ O* + H^+ + e^-) for both the FM and G-type AFM $LaFeO_3$(001) BO_2 surface, despite the ΔE(HO*) of the FM $LaFeO_3$ is much stronger than that of G-type AFM $LaFeO_3$. This is due to the ~0.4 eV positive deviation of ΔE(O*) from the ΔE(O*) vs. ΔE(HO*) linear correlation (Figure 5), which shifts the FM $LaFeO_3$ (001) BO_2 surface from the left branch of the volcano to the right branch. As a result, FM $LaFeO_3$ is only slightly more active (with ~0.1 V lower (over)potential) than the G-type AFM $LaFeO_3$ for OER.

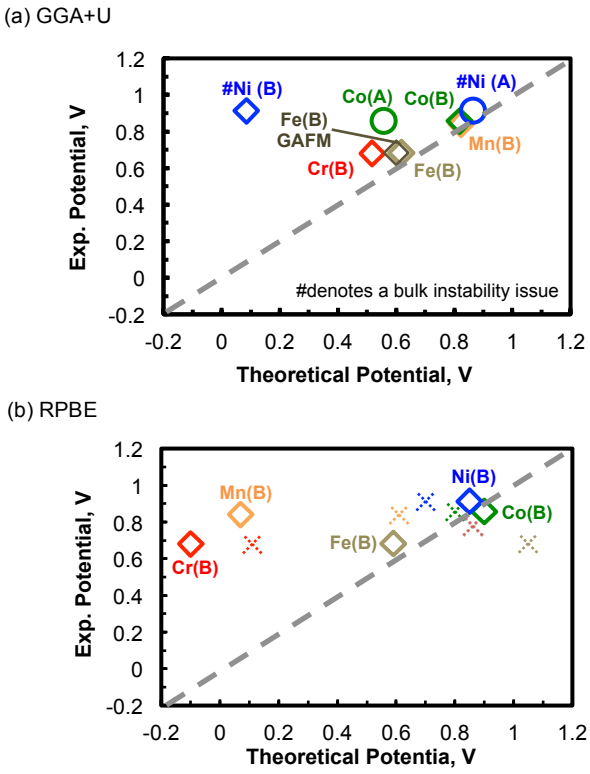

Figure 9. Experimental ORR potentials (measured using catalyst ink prepared by mixing perovskite oxide powders and acetylene black carbon with tetrahydrofuran and an appropriate amount of neutralized Nafion)[5, 68] vs. theoretical perovskite $LaBO_3$ (B=Cr, Mn, Fe (both GAFM and FM), Co, and Ni) ORR potentials calculated with (a) GGA+U with U_{eff}s for *d*-electrons of transition metal elements from Ref. 19. For simplicity, only transition elements are labeled to represent the perovskite systems. A and B in parenthesis indicate the predicted ORR potentials on the bare (001) AO and BO_2 surface termination, respectively. All the perovskites (001) slabs are modeled using the ferromagnetic state, and an additional G-type AFM (001) BO_2 slabs are included for $LaFeO_3$, due to the high T_N (= ~740 K) of $LaFeO_3$ system. The predicted ORR potentials are obtained based on the reaction free energies volcano plot shown in Figure 6(c). Taking into account and the surface stability analysis results shown in Figure 3, the (001) bare surfaces of perovskites were predicted to be less stable surfaces than the H* covered or HO* covered (001) surfaces under the ORR condition, as indicated by the use of empty symbols. The dashed lines represent the best fit to the experimental results. (b) the RPBE predictions (data from Ref. 14), where the solid symbols contain additional solvation free energy correction terms for adsorbed HO*, O*, and HOO* from Ref. 46, while the cross symbols represent the RPEB results without the solvation free energy corrections (*i.e.* corresponds to the predicted OER potentials in Ref. 14).

Similarly, for $LaFeO_3$ ORR the optimal $\Delta G(HO^*)$ is located between those of the FM vs. the G-type AFM $LaFeO_3$ (001) BO_2 surface, leading to the comparable theoretical ORR activities between the two magnetic arrangements of the (001) BO_2 surfaces. On the other hand, the HO* adsorption energies were found to be close on the (001) bare AO surfaces between the FM and G-type AFM $LaFeO_3$ ($\Delta G(HO^*)$ = -0.67 eV/HO* for FM vs. -0.77 eV/HO* for G-type AFM, both relative to the H_2/H_2O reference at 0V vs. RHE), whereas the sub-surface layer O *2p*-band centers were also found to be located at similar energy level relative to their Fermi energy (-3.41 eV for the FM state and -3.47 eV for G-type AFM). The stronger binding on the AO surfaces can be attributed the electron doping nature of the AO surfaces and Fermi level pinning near the AO surfaces of $LaFeO_3$ with a band gap (~2 eV for the $LaFeO_3$ bulk), which downshifts the O *2p*-band relative to the Fermi level near the AO surfaces[27]. At high coverage of $LaFeO_3$ (001) AO surfaces (θ=0.75 ML), both predicted ORR activities were also found to be close (0.3 V for G-type AFM and 0.5 V for FM based on the $\Delta G(HO^*)$ as shown in Figure 10. While our results indicated the G-type AFM $LaFeO_3$ may possess distinct surface adsorption properties between the two (001) counter surfaces, *i.e.*, the AO termination exhibits stronger HO* binding and the BO_2 surfaces exhibit a weak HO* binding, their resulting ORR potentials were coincidentally shown to be close. Again, in this work we did not attempt to resolve the surface magnetic states for surface adsorption properties between FM and G-type AFM, and further work is needed in this area.

5. The role of the coverage dependent surface adsorption on the predicted ORR activities

The construction of the OER and ORR volcanoes and the predicted theoretical potentials of the perovskite (001) surfaces discussed in Section D.4.2 and Section D.4.3 were based on adsorption energies on bare surfaces, which was assumed to be a good approximation to adsorption on the equilibrium coverage surface based on the weak coverage dependence in the surface adsorption energies revealed in Figure S1. However, there are also exceptions such as $LaCrO_3$, $LaMnO_3$, and $LaFeO_3$ (001) AO surfaces that exhibit strong or moderate surface coverage dependence on their adsorption energies of the OER/ORR reaction intermediates. In particular, the $LaCrO_3$ and $LaFeO_3$ (001) AO surfaces with 1ML HO* coverage were shown to be the stable surfaces than their (001) BO_2 surfaces under the ORR condition (Figure 3), which are indeed important to take into account. Furthermore,, the (001) BO_2 surfaces with adsorbed H* were shown to be the more stable surfaces than their bare BO_2 surfaces among the investigated ones under the ORR conditions for $LaMnO_3$(0.5ML H*), $LaFeO_3$(0.5~0.75ML H*), $LaCoO_3$(0.5ML H*), and $LaNiO_3$ (1ML H*), as summarized in Table 2 and shown in Figure S2, Supporting Information. We then focused on the ORR voltage condition to investigate the effect of the coverage dependence in the predicted theoretical ORR potentials. Note that for coverage dependence on the predicted ORR activities we consider both the GAFM and FM states for $LaFeO_3$. We do not perform the same analysis for the OER voltage condition as $LaCrO_3$ and $LaMnO_3$ suffers from the bulk instability issues under the OER conditions (Figure 2), where $LaCrO_3$ is unstable relative to the Cr phases at higher oxidation states and $LaMnO_3$ may be further stabilized with cation vacancies, thereby the surface stability analysis including the stable coverage may have to be further refined. Consequently, the even narrower experimental OER potential window among $LaMnO_3$, $LaFeO_3$, $LaCoO_3$, and $LaNiO_3$ (smaller than 0.1 V[4]) is very difficult to be meaningfully resolved within the adopted DFT modeling approaches in this work. Therefore, for predicting the OER activities, we only focused on the surfaces with weak coverage dependent binding energies (generally BO_2 except for $LaNiO_3$

 This journal is © The Royal Society of Chemistry 2012

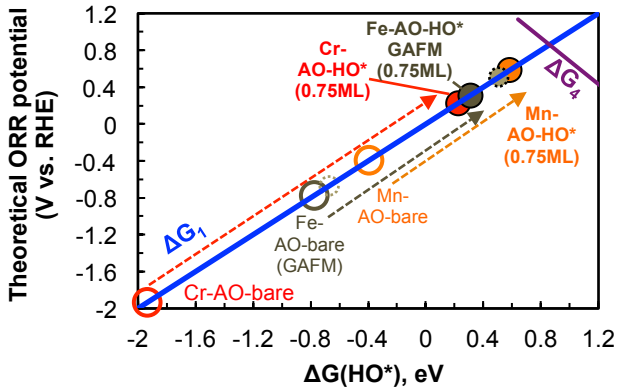

Figure 10. The coverage effect on the predicted ORR potential for the $LaCrO_3$ (red), $LaMnO_3$ (orange), and $LaFeO_3$ (GAFM: deep olive with solid circles; FM: light olive with dotted circles) (001) AO surface in the theoretical ORR volcano plot, where ΔG_1 (blue line) is the reaction free energy of $H_2O(l) + * \leftrightarrows HO^* + H^+ + e^-$ and ΔG_4 (purple line) is the reaction free energy of $HOO^* \leftrightarrows O_2(g) + H^+ + e^-$. The empty circles represents the adsorption energies calculated at low coverage (relative to the bare AO surface, *i.e.* $\theta = 0$), while the filled circles represent the adsorption energies calculated at high coverage (relative to $\theta = 0.75$). For $LaFeO_3$, the ground state G-type AFM results was selected to represent the ORR activity of the $LaFeO_3$ with labeling, while olive circles with dotted lines and without labeling are for the FM results.

which is AO, as shown in Figure S1) and we assumed these surfaces can be used to represent the observed catalytic properties, since both the (001) AO and BO_2 surfaces of the $LaBO_3$ perovskites covered with the stable adsorbates were shown to be competitively stable under the OER conditions(Figure 4).

The $LaCrO_3$, $LaMnO_3$, and $LaFeO_3$ (001) AO surfaces with strong coverage dependent surface adsorption properties were shown to be stable with 1ML HO* (Table 2 and Figure 3). These surfaces were assessed for the ORR reaction cycle constructed with the HO* covered (001) AO surface at $\theta = 0.75$, where 1 out of the 4 surface adsorption sites is available for replacement of the HO*, O*, and HOO* while the other 3 sites are all occupied by HO*. We note these surface adsorption energies were computed at a given surface coverage, *i.e.*, using the reference energy of the HO* covered (001) AO surface at $\theta = 0.75$, which is different from the averaged surface adsorption energy results shown in Figure S1 that are computed relative to the bare (001) surfaces. In Figure 10, we showed the effect of including the coverage effects on the predicted ORR activities of the $LaCrO_3$, $LaMnO_3$, and $LaFeO_3$ (001) AO surface in the ORR volcano plot. We note that on the strong binding branch of the ORR volcano plot, the HO* adsorption is the rate limiting reaction and the ORR activity of the bare AO surface is predicted to be very low due to the too strong binding of HO* simulated at the low coverage. However, upon increasing surface HO* coverage to its stable value, the predicted ORR voltages increase by 1~2 V (Figure 10).

Similarly to the OH* effects on AO surfaces, we then considered the effects of H* surface coverage on BO_2 surfaces. The HO* adsorption energies were calculated at the stable H* coverage of BO_2 surfaces under the ORR conditions, as indicated in Figure 3. These HO* adsorption energies were found to be different by up to 0.4 eV/HO* compared to those computed at the bare BO_2 surfaces, as shown in Figure S7, Supporting Information. The predicted ORR activities of the stable (001) BO_2 surfaces with partial H* coverage were found to change by just 0.2 V compared to the bare surfaces for $LaMnO_3$, $LaFeO_3$, and $LaCoO_3$, and by 0.4 V for $LaNiO_3$, where the larger value for Ni is in part due to its full coverage with 1ML of H*.

Results from a full assessment for the predicted ORR activities based on the stable coverage of the perovskite (001) surfaces were provided in Figure 11(a), along with a comparison between the theoretical ORR potentials at the stable coverage vs. the experimental ORR potentials reported in Ref. [5] shown in Figure 11(b). This figure contains all the effects of coverage and GGA+U and therefore shows the best values from our approach for the ORR. We note by taking into account stable surface coverage, both the stable AO and BO_2 surfaces were predicted to have a closer ORR activity window (within 0.2~0.3 V). Our predictions is also supported by the experimental measurements of the $La_{1-x}Sr_xMnO_3$ epitaxial thin films[69], where surface terminations and orientations were found to lead to no strong influence on the measured ORR activities. Another notable effect of the coverage is that the activity of the $LaNiO_3$ (001) AO bare surface, which is predicted to be located close to the top of the ORR volcano, is shifted to be lower than $LaCoO_3$ when including the stable 0.25ML H* coverage. Furthermore, the bulk stability phase diagram in Figure 2 suggests $LaNiO_3$ is not stable with respect to the binary metal oxides. It is well known that the $LaNiO_3$ may decompose to form Ruddlesden-Popper phases upon increasing temperature and lowering oxygen partial pressure (which corresponds to decrease of oxygen chemical potential)[70]. To further examine $LaNiO_3$ bulk instability issue, we performed the bulk stability analysis for $LaNiO_3$ relative to the formation of the Ruddlesden-Popper phases (with NiO and O_2) vs. applied potential. As shown in Figure S8, the $LaNiO_3$ becomes less stable upon lowering the applied potential, and is predicted to favor the reaction of decomposing $LaNiO_3$ to form the Ruddlesden-Popper phases in the ORR condition (0.8~0.9 V). As the measured ORR activity of the $La_4Ni_3O_{10}$ in Ref. [5] is lower than $LaMnO_3$ and $LaCoO_3$, It is likely such a phase instability issue in bulk or near surface $LaNiO_3$ can also be associated with the lower $LaNiO_3$ ORR activity reported in Ref. [71] vs. the high ORR activity reported in Ref. [5], in addition to the synergistic activity-enhancement effect from combination of $LaNiO_3$ and carbon proposed in Ref. [71]. Overall, the GGA+U method predicted the ORR activity trend vs. the $LaBO_3$ series to be in the following order Co>Mn≈Ni>Fe>Cr at their stable coverage, in good agreement with the experimental ORR activity trends[5, 71]. However, Ni shows instabilities under the ORR conditions, so it is not clear how meaningful the agreement is for the comparison of $LaNiO_3$ ORR activity between the experimental activity measurement and the theoretical prediction, while our self-consistent thermodynamic analysis provided additional insights and information regarding surface stability and coverage.

(a)

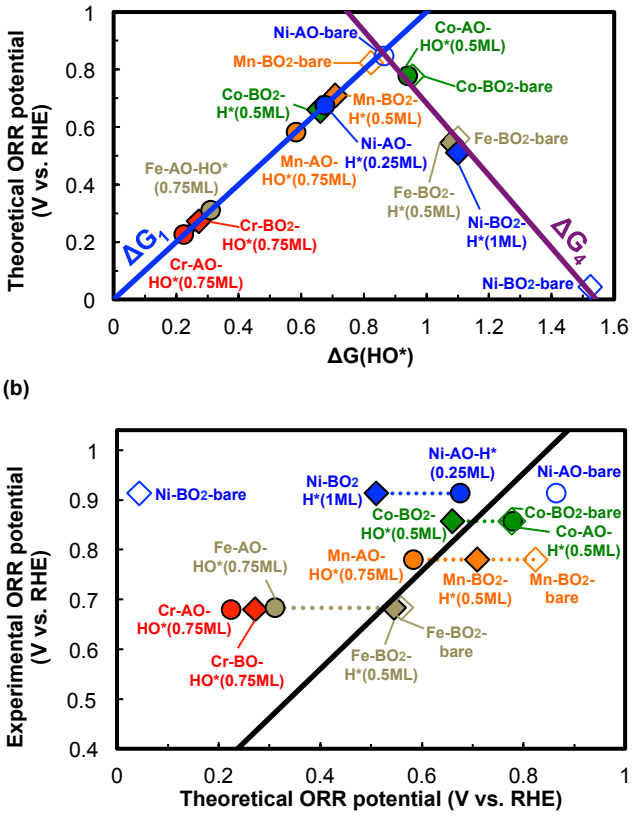

Figure 11. (a) The theoretical ORR volcano plot, where ΔG_1 (blue line) is the reaction free energy of $H_2O(l) + * \leftrightarrows HO^* + H^+ + e^-$ and ΔG_4 (purple line) is the reaction free energy of $HOO^* \leftrightarrows O_2(g) + H^+ + e^-$, for $LaBO_3$ perovskite (B=Cr (red), Mn (orange), Fe-GAFM (olive), Co (green) and Ni (blue)) (001) AO (circles) and BO_2 (diamonds) surfaces at the stable surface coverage summarized in Table 2. For each transition metal perovskite system, the solid symbols correspond to the stable adsorbate covered (001) AO and BO_2 surfaces (Figure 3 and Table 2) with comparably thermodynamic stability, while the empty symbols represent the results of the less stable (001) bare surfaces shown in Figure 9(a). (b) Comparison between the theoretical ORR potentials vs. the experimental ORR potentials from Ref. 5(V vs. RHE) of the investigated $LaBO_3$ perovskite (001) surfaces at the stable coverage summarized in Table 2. The black thick line is mainly for guiding purpose with a slope of 1.

E. Conclusions

In this study, we have utilized the DFT-GGA+U method to self-consistently predict the ORR and OER activities of $LaBO_3$ (B=Cr, Mn, Fe, Co, and Ni) (001) surfaces at stable surface coverage under the ORR/OER conditions in alkaline solution within the concerted proton-electron transfer scheme[29]. In our DFT surface modeling, we demonstrated that the bare (001) AO surfaces generally bind oxidizing species more strongly than the bare BO_2 surfaces. To explain these differences we observed that charge doping on the two surfaces originating from surface polarity compensation caused opposite surface band bending. This band bending difference can be seen through the observation of a lower O *2p*-band center relative to the Fermi level near the electron doped (001) AO surfaces and a higher O *2p*-band relative to the Fermi level near the hole doped (001) BO_2 surfaces, which has been shown to correlate with surface oxygen binding and stability of bulk and surface oxygen defect formation across a wide range of systems[27, 58]. We further demonstrated the surface HO* adsorption energies of the $LaBO_3$ (001) AO and BO_2 bare surfaces correlate linearly with their sub-surface layer (2nd surface layer) oxygen *2p*-band centers, as the opposite surface band bending leads to the upshift and downshift of the oxygen *2p*-band center relative to the Fermi level near the BO_2 surfaces and the AO surfaces vs. the bulk, respectively, and therefore result in the observed binding energy difference between the two counter surface terminations.

In our surface stability analysis, we showed that the stable $LaBO_3$ (001) AO and BO_2 surfaces are mostly covered with adsorbates under the ORR and OER conditions, where the most stable adsorbed species and their coverage depend on the applied potentials vs. RHE:

- For the ORR condition (~0.83 V vs. RHE), our surface stability analysis predicts that OH* and H* are most stable on (001) AO and BO_2 surfaces, respectively, for all systems except $LaNiO_3$, where H* is stabilized on both surfaces. Our surface stability analysis was then performed taking proper coverages into account. The stability results suggested that under ORR conditions the (001) AO surfaces are stable for $LaCrO_3$ and $LaFeO_3$, while both the (001) AO and BO_2 surfaces are both about equally stable for $LaMnO_3$, $LaCoO_3$ and $LaNiO_3$. We also found that under ORR conditions the $LaNiO_3$ bulk was unstable relative to formation of the more reduced Ruddlesden-Popper and NiO phases in our bulk stability analysis, indicating instability of $LaNiO_3$ for ORR.

- Under OER conditions (~1.63 V vs. RHE) we found that the oxidizing adsorbate (HO*/HOO* or O*) fully covered (001) AO and BO_2 surfaces are both about equally stable for all the investigated $LaBO_3$ systems except $LaNiO_3$, where the AO surfaces covered with HO* is still more stable. In addition, the bulk stability and surface stability analysis suggests $LaCrO_3$ and $LaMnO_3$ are likely to be chemically (form other stable phases) or structurally (formed cation vacancies) modified near the surfaces under the OER conditions.

The predicted OER and ORR thermodynamic overpotentials in this work performed using the GGA+U method and the stable surface coverage showed reduced absolute error vs. the previously reported experimental ORR/OER activities done without +U or similar corrections for correlated electron errors in DFT[4, 5]. In addition, our results suggested while inherent stronger binding nature of the bare AO surface termination vs. the bare BO_2 surface may indicate the inactiveness of the AO surface, the stable adsorbate covered AO surfaces can become comparatively active vs. the stable BO_2 surfaces for ORR when taking into account their stable coverage.

Overall, the GGA+U OER activity trend for the (001) surfaces of the $LaBO_3$ series were revealed to be in the following order Ni>Fe≈Co≈Mn>Cr*. While the GGA+U approach led to an improved accuracy of the predicted OER overpotentials it also led to a less clear trend between theoretically predicted vs. experimentally measured activities[4] among the $LaBO_3$ (B=Cr~Ni) compounds. The lack of a clear trend is not

 This journal is © The Royal Society of Chemistry 2012

surprising due to the narrow experimental potential window in which the Mn, Fe, and Co compounds reside (within 0.1 V), which is likely within to the energetic resolution limit of the adopted *ab initio* thermodynamic framework (0.1~0.2 eV)[19] as well as model assumptions and approximations. In addition, the stability issue of $LaCrO_3$ and formation of the cation vacancies in $LaMnO_3$ at high potentials suggest further refinement of the bulk metal chemical potential references is needed for assessing the surface stability under the OER conditions. In contrast, although the experimental ORR potential window is also small for the perovskites, the GGA+U method predicted the overall ORR activity trend vs. the $LaBO_3$ series to be in the following order Co>Mn≈Ni>Fe>Cr, consistent with the experimental ORR activity trends[5, 71]. Specifically, the predicted relative ORR activities among all the stable $LaBO_3$ (001) surfaces were shown to be in the following order: Co-AO with 0.5 ML HO* > Mn-BO_2 with 0.5 H* > Ni- AO with 0.25ML H* > Co-BO_2 with 0.5 ML H*> Mn-AO with 1ML HO* > Ni-BO_2 with 1ML H*> Fe-BO_2 with 0.5 ML H* > Fe-AO with 1 ML HO*> Cr-BO_2 with 1ML HO* > Cr-AO with 1ML HO*. The greater success for the ORR vs. OER predictions may be in part due to our performing self-consistent assessment for the theoretical ORR activities at the stable (001) surfaces and surface coverages. These surface coverage studies yielded interesting new understanding. In particular, we demonstrated that the coverage dependent surface adsorption of the $LaCrO_3$, $LaMnO_3$, and $LaFeO_3$ (001) AO surface can result in weaker HO* adsorption strength at high coverage of HO* and therefore more active ORR activities than those predicted at low coverage, as well as much closer predicted ORR activities between the (001) AO and BO_2 surfaces at their stable coverage.

Our result demonstrated that the *ab initio* thermodynamic approaches adopted in this work can integrate surface stability, surface coverage, and OER/ORR potential prediction to yield understanding of their coupling and predictions of activity. These results can be effectively compared with experimental characterizations/measurements to unveil surface structure-functionality relationship across a wide range of potentials in order to yield insights for rational development of perovskite OER and ORR catalysts.

Acknowledgements

We gratefully e gratefully acknowledge financial support for 40% of Yueh-Lin Lee's effort on this work from the Department of Energy (DOE), National Energy Technology Laboratory (NETL), Solid State Energy Conversion Alliance (SECA) Core Technology Program (Funding Opportunity Number DEFE0009435). Funding for Dane Morgan, Milind Gadre, and partial funding (approximately 10%) for Yueh-Lin Lee for this work was provided by the NSF Software Infrastructure for Sustained Innovation (SI2) award No. 1148011. Funding for Yang Shao-Horn and 40% of funding for Yueh-Lin Lee was given by the Skoltech-MIT Center for Electrochemical Energy. Computational support was provided by a NERSC allocation from the Center for Nanophase Materials Sciences (CNMS) at Oak Ridge National Laboratory under grant number CNMS2013-292.

Notes and references

[a] Electrochemical Energy Laboratory, Massachusetts Institute of Technology, Cambridge, Massachusetts 02139, United States.

[b] Department of Materials Science and Engineering, Massachusetts Institute of Technology, Cambridge, Massachusetts 02139, United States.

[c] Department of Mechanical Engineering, Massachusetts Institute of Technology, Cambridge, Massachusetts 02139, United States.

[d] Department of Materials Science and Engineering, University of Wisconsin-Madison, Madison, Wisconsin 53706, United States.

† Footnotes should appear here. These might include comments relevant to but not central to the matter under discussion, limited experimental and spectral data, and crystallographic data.

Electronic Supplementary Information (ESI) available: [details of any supplementary information available should be included here]. See DOI: 10.1039/b000000x/

1 Citations here in the format A. Name, B. Name and C. Name, *Journal Title*, 2000, **35**, 3523; A. Name, B. Name and C. Name, *Journal Title*, 2000, **35**, 3523.

1. J. O. M. Bockris and T. Otagawa, *Journal of the Electrochemical Society*, 1984, 131, 290-302.
2. M. W. Kanan and D. G. Nocera, *Science*, 2008, 321, 1072-1075.
3. K. A. Stoerzinger, M. Risch, J. Suntivich, W. M. Lu, J. Zhou, M. D. Biegalski, H. M. Christen, Ariando, T. Venkatesan and Y. Shao-Horn, *Energy & Environmental Science*, 2013, 6, 1582-1588.
4. J. Suntivich, K. J. May, H. A. Gasteiger, J. B. Goodenough and Y. Shao-Horn, *Science*, 2011, 334, 1383-1385.
5. J. Suntivich, H. A. Gasteiger, N. Yabuuchi, H. Nakanishi, J. B. Goodenough and Y. Shao-Horn, *Nat. Chem.*, 2011, 3, 546-550.
6. A. Grimaud, K. J. May, C. E. Carlton, Y.-L. Lee, M. Risch, W. T. Hong, J. Zhou and Y. Shao-Horn, *Nature Communications*, 2013, 4.
7. J. K. Norskov, T. Bligaard, J. Rossmeisl and C. H. Christensen, *Nat. Chem.*, 2009, 1, 37-46.
8. A. Vojvodic and J. K. Nørskov, *Science*, 2011, 334, 1355-1356.
9. S. Trasatti, *Journal of Electroanalytical Chemistry and Interfacial Electrochemistry*, 1980, 111, 125-131.
10. Y. Matsumoto, J. Kurimoto and E. Sato, *Journal of Electroanalytical Chemistry and Interfacial Electrochemistry*, 1979, 102, 77-83.
11. F. Calle-Vallejo, O. A. Díaz-Morales, M. J. Kolb and M. T. M. Koper, *ACS Catalysis*, 2015, 5, 869-873.
12. S. H. Chang, N. Danilovic, K.-C. Chang, R. Subbaraman, A. P. Paulikas, D. D. Fong, M. J. Highland, P. M. Baldo, V. R. Stamenkovic, J. W. Freeland, J. A. Eastman and N. M. Markovic, *Nature Communications*, 2014, 5.
13. K. A. Stoerzinger, L. Qiao, M. D. Biegalski and Y. Shao-Horn, *The Journal of Physical Chemistry Letters*, 2014, 5, 1636-1641.
14. I. C. Man, H.-Y. Su, F. Calle-Vallejo, H. A. Hansen, J. I. Martínez, N. G. Inoglu, J. Kitchin, T. F. Jaramillo, J. K. Nørskov and J. Rossmeisl, *ChemCatChem*, 2011, 3, 1159-1165.
15. Y. Wang and H.-P. Cheng, *The Journal of Physical Chemistry C*, 2013, 117, 2106-2112.
16. J. Rossmeisl, Z. W. Qu, H. Zhu, G. J. Kroes and J. K. Norskov, *Journal of Electroanalytical Chemistry*, 2007, 607, 83-89.
17. B. Hammer, L. B. Hansen and J. K. Nørskov, *Physical Review B*, 1999, 59, 7413-7421.
18. V. I. Anisimov, J. Zaanen and O. K. Andersen, *Physical Review B*, 1991, 44, 943-954.
19. L. Wang, T. Maxisch and G. Ceder, *Physical Review B*, 2006, 73, 195107.
20. S. Lutfalla, V. Shapovalov and A. T. Bell, *Journal of Chemical Theory and Computation*, 2011, 7, 2218-2223.
21. J. Heyd, G. E. Scuseria and M. Ernzerhof, *The Journal of Chemical Physics*, 2006, 124, 219906-219901.

22. M. García-Mota, M. Bajdich, V. Viswanathan, A. Vojvodic, A. T. Bell and J. K. Nørskov, *The Journal of Physical Chemistry C*, 2012, 116, 21077-21082.
23. H. A. Hansen, J. Rossmeisl and J. K. Norskov, *Physical Chemistry Chemical Physics*, 2008, 10, 3722-3730.
24. K. A. Stoerzinger, W. T. Hong, G. Azimi, L. Giordano, Y.-L. Lee, E. J. Crumlin, M. D. Biegalski, H. Bluhm, K. K. Varanasi and Y. Shao-Horn, *submitted*, 2015.
25. K. J. May, C. E. Carlton, K. A. Stoerzinger, M. Risch, J. Suntivich, Y.-L. Lee, A. Grimaud and Y. Shao-Horn, *The Journal of Physical Chemistry Letters*, 2012, 3, 3264-3270.
26. J. Goniakowski, F. Finocchi and C. Noguera, *Rep. Prog. Phys.*, 2008, 71.
27. Y.-L. Lee and D. Morgan, *Physical Review B*, 2015, 91, 195430.
28. J. K. Norskov, J. Rossmeisl, A. Logadottir, L. Lindqvist, J. R. Kitchin, T. Bligaard and H. Jonsson, *The Journal of Physical Chemistry B*, 2004, 108, 17886-17892.
29. M. T. M. Koper, *Chemical Science*, 2013, 4, 2710-2723.
30. G. Kresse and J. Furthmuller, *Physical Review B*, 1996, 54, 11169-11186.
31. J. P. Perdew, K. Burke and M. Ernzerhof, *Physical Review Letters*, 1996, 77, 3865-3868.
32. G. Kresse and D. Joubert, *Physical Review B*, 1999, 59, 1758-1775.
33. S. L. Dudarev, G. A. Botton, S. Y. Savrasov, C. J. Humphreys and A. P. Sutton, *Physical Review B*, 1998, 57, 1505-1509.
34. Y.-L. Lee, J. Kleis, J. Rossmeisl and D. Morgan, *Physical Review B (Condensed Matter and Materials Physics)*, 2009, 80, 224101.
35. N. Furuhata, E. Nakamura and E. Sawaguchi, Springer-Verlag, Berlin, 1969.
36. J. B. Goodenough, *Physical Review*, 1967, 164, 785-789.
37. J. Neugebauer and M. Scheffler, *Physical Review B*, 1992, 46, 16067-16080.
38. K. Johnston, M. R. Castell, A. T. Paxton and M. W. Finnis, *Physical Review B*, 2004, 70, 085415.
39. S. Piskunov, E. Heifets, T. Jacob, E. A. Kotomin, D. E. Ellis and E. Spohr, *Physical Review B*, 2008, 78, 121406(R).
40. D. Lee, Y.-L. Lee, W. T. Hong, M. D. Biegalski, D. Morgan and Y. Shao-Horn, *Journal of Materials Chemistry A*, 2015, 3, 2144-2157.
41. J. W. Johnson, E. H. Oelkers and H. C. Helgeson, *Computers & Geosciences*, 1992, 18, 899-947.
42. B. Beverskog and I. Puigdomenech, *Corrosion Science*, 1997, 39, 43-57.
43. M. Pourbaix, *Atlas of Electrochemical Equilibria in Aqueous Solutions*, National Association of Corrosion Engineers, 1974.
44. K. A. Persson, B. Waldwick, P. Lazic and G. Ceder, *Physical Review B*, 2012, 85, 235438.
45. I. Castelli, K. Thygesen and K. Jacobsen, *Topics in Catalysis*, 2014, 57, 265-272.
46. Y. Sha, T. H. Yu, Y. Liu, B. V. Merinov and W. A. Goddard, *The Journal of Physical Chemistry Letters*, 2010, 1, 856-861.
47. L.-P. Wang, Q. Wu and T. Van Voorhis, *Inorganic Chemistry*, 2010, 49, 4543-4553.
48. L.-P. Wang and T. Van Voorhis, *The Journal of Physical Chemistry Letters*, 2011, 2, 2200-2204.
49. J. Rossmeisl, J. K. Nørskov, C. D. Taylor, M. J. Janik and M. Neurock, *The Journal of Physical Chemistry B*, 2006, 110, 21833-21839.
50. V. Tripković, E. Skúlason, S. Siahrostami, J. K. Nørskov and J. Rossmeisl, *Electrochimica Acta*, 2010, 55, 7975-7981.
51. Z. Xu and J. R. Kitchin, *The Journal of Physical Chemistry C*, 2014.
52. M. M. Montemore and J. W. Medlin, *Catalysis Science & Technology*, 2014, 4, 3748-3761.
53. K. A. Stoerzinger, W. T. Hong, E. J. Crumlin, H. Bluhm, M. D. Biegalski and Y. Shao-Horn, *The Journal of Physical Chemistry C*, 2014, 118, 19733-19741.
54. J. O. Bockris and T. Otagawa, *The Journal of Physical Chemistry*, 1983, 87, 2960-2971.
55. B. C. Tofield and W. R. Scott, *Journal of Solid State Chemistry*, 1974, 10, 183-194.
56. Y.-L. Lee and D. Morgan, *Physical Chemistry Chemical Physics*, 2012, 14, 290-302.
57. X. Rong and A. M. Kolpak, *The Journal of Physical Chemistry Letters*, 2015, 6, 1785-1789.
58. Y.-L. Lee, J. Kleis, J. Rossmeisl, Y. Shao-Horn and D. Morgan, *Energy & Environmental Science*, 2011, 4, 3966-3970.
59. V. L. Chevrier, S. P. Ong, R. Armiento, M. K. Y. Chan and G. Ceder, *Physical Review B*, 2010, 82, 075122.
60. F. Zhou, M. Cococcioni, C. A. Marianetti, D. Morgan and G. Ceder, *Physical Review B*, 2004, 70, 235121.
61. M. T. M. Koper, *Journal of Electroanalytical Chemistry*, 2011, 660, 254-260.
62. B. Hammer and J. K. Norskov, *Nature*, 1995, 376, 238-240.
63. F. Calle-Vallejo, N. G. Inoglu, H.-Y. Su, J. I. Martinez, I. C. Man, M. T. M. Koper, J. R. Kitchin and J. Rossmeisl, *Chemical Science*, 2013, 4, 1245-1249.
64. H. J. Kulik, M. Cococcioni, D. A. Scherlis and N. Marzari, *Physical Review Letters*, 2006, 97, 103001.
65. J. Winkler and H. Gray, in *Molecular Electronic Structures of Transition Metal Complexes I*, eds. D. M. P. Mingos, P. Day and J. P. Dahl, Springer Berlin Heidelberg, 2012, vol. 142, ch. 55, pp. 17-28.
66. H. Kang and J. L. Beauchamp, *Journal of the American Chemical Society*, 1986, 108, 5663-5668.
67. E. A. Carter and W. A. Goddard, *The Journal of Physical Chemistry*, 1988, 92, 2109-2115.
68. J. Suntivich, H. A. Gasteiger, N. Yabuuchi and Y. Shao-Horn, *Journal of The Electrochemical Society*, 2010, 157, B1263-B1268.
69. K. A. Stoerzinger, W. Lü, C. Li, Ariando, T. Venkatesan and Y. Shao-Horn, *The Journal of Physical Chemistry Letters*, 2015, 6, 1435-1440.
70. M. Zinkevich and F. Aldinger, *Journal of Alloys and Compounds*, 2004, 375, 147-161.
71. J. Sunarso, A. A. J. Torriero, W. Zhou, P. C. Howlett and M. Forsyth, *The Journal of Physical Chemistry C*, 2012, 116, 5827-5834.

 This journal is © The Royal Society of Chemistry 2012